JGR Solid Earth

RESEARCH ARTICLE
10.1029/2021JB022304

Illuminating the Pre-, Co-, and Post-Seismic Phases of the 2016 M7.8 Kaikōura Earthquake With 10 Years of Seismicity

C. J. Chamberlain[1], W. B. Frank[2], F. Lanza[3], J. Townend[1], and E. Warren-Smith[4]

[1]School of Geography, Environment and Earth Sciences, Victoria University of Wellington, Wellington, New Zealand, [2]Department of Earth, Atmospheric and Planetary Sciences, Massachusetts Institute of Technology, Cambridge, MA, USA, [3]Swiss Seismological Service, ETH Zürich, Zürich, Switzerland, [4]GNS Science, Lower Hutt, New Zealand

Key Points:

- 10-year long matched-filter derived catalog of 33,328 earthquakes surrounding the 2016 Kaikōura earthquake
- Observed offshore reverse faulting provides a direct and viable rupture pathway
- No detectable seismicity occurs on the subduction interface, and any deformation there is aseismic

Supporting Information:

Supporting Information may be found in the online version of this article.

Correspondence to:

C. J. Chamberlain,
calum.chamberlain@vuw.ac.nz

Citation:

Chamberlain, C. J., Frank, W. B., Lanza, F., Townend, J., & Warren-Smith, E. (2021). Illuminating the pre-, co-, and post-seismic phases of the 2016 M7.8 Kaikōura earthquake with 10 years of seismicity. *Journal of Geophysical Research: Solid Earth*, *126*, e2021JB022304. https://doi.org/10.1029/2021JB022304

Received 24 APR 2021
Accepted 18 JUL 2021

Abstract The 2016 M7.8 Kaikōura earthquake is one of the most complex earthquakes in recorded history, with significant rupture of at least 21 crustal faults. Using a matched-filter detection routine, precise cross-correlation pick corrections, and accurate location and relocation techniques, we construct a catalog of 33,328 earthquakes between 2009 and 2020 on and adjacent to the faults that ruptured in the Kaikōura earthquake. We also compute focal mechanisms for 1,755 of the earthquakes used as templates. Using this catalog we reassess the rupture pathway of the Kaikōura earthquake. In particular we show that: (a) the earthquake nucleated on the Humps Fault; (b) there is a likely linking offshore reverse fault between the southern fault system and the Papatea Fault, which could explain the anomalously high slip on the Papatea Fault; (c) the faults that ruptured in the 2013 Cook Strait sequence were reactivated by the Kaikōura earthquake and may have played a role in the termination of the earthquake; and (d) no seismicity on an underlying subduction interface is observed beneath almost all of the ruptured region suggesting that if deformation did occur on the plate interface then it occurred aseismically and did not play a significant role in generating co-seismic ground motion.

Plain Language Summary The 2016 Kaikōura earthquake in the South Island of New Zealand, is one of the most complex earthquakes reported. While extensive geological work has been undertaken to map the surface faulting in the earthquake, it remains unclear how these faults are linked together at depth. In this paper we document the construction of a dense, long-duration catalog of earthquakes that occurred on and around the faults that slipped in the Kaikōura earthquake. Using this catalog of 33,328 earthquakes we are able to illuminate likely sub-surface links between faults and investigate how these faults slipped before and after the Kaikōura earthquake. We show that offshore faults provide a link between the southern faults, where the earthquake started, and the northern faults, where the highest slip occurred. We also show that the earthquake stopped on faults that had previously slipped in the 2013 Cook Strait earthquakes, and which likely played a role in earthquake arrest. Finally we see no evidence for elevated seismicity on the underlying subduction interface beneath the faults that slipped in the Kaikōura earthquake.

1. Introduction

The November 2016 Kaikōura M 7.8 earthquake ruptured at least 21 faults in the Marlborough Fault Zone at the transition from subduction on the Hikurangi subduction zone to on-land transpression (Figure 1; Hamling et al., 2017; Kaiser et al., 2017; Litchfield et al., 2018). This complex earthquake involved a wide range of co-seismic faulting styles, producing dextral, sinistral, reverse and normal surface ruptures (Clark et al., 2017). In addition to the extensive crustal faulting, the underlying subduction interface may have slipped co-seismically (Bai et al., 2017; T. Wang et al., 2018), although regional data show little evidence for this (Hamling et al., 2017; Holden et al., 2017).

The transpressional rupture cascade resulted in significant surface rupture of multiple previously known and unknown faults (Litchfield et al., 2018). The complexity of the earthquake rupture (Hamling et al., 2017) has to date precluded the robust constraint of the role of individual faults within the rupture sequence (e.g., Holden et al., 2017) and the dynamics of the rupture propagation and termination (Ando & Kaneko, 2018; Ulrich et al., 2019). When modeling such complex ruptures, the identification of all major participating

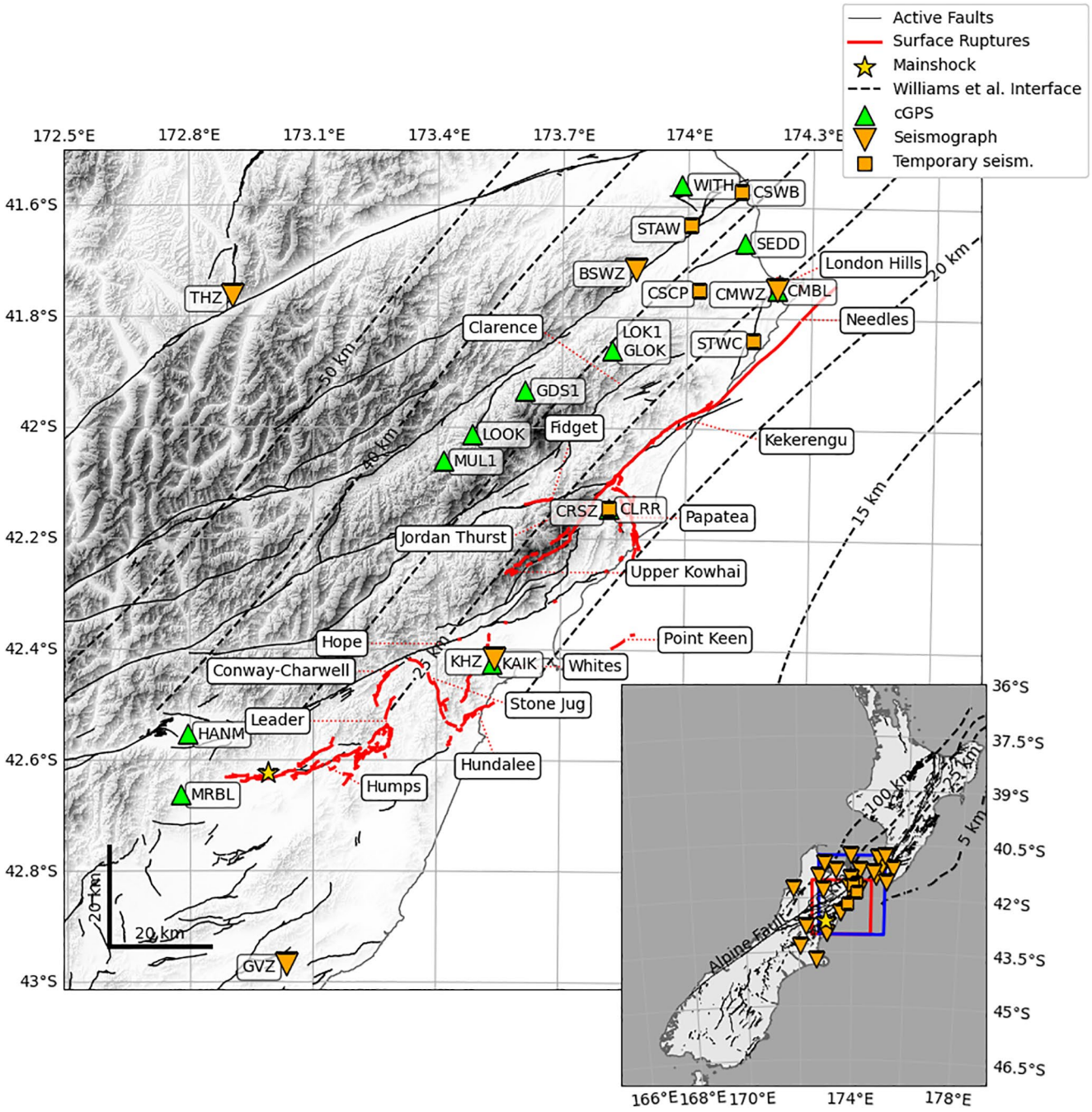

Figure 1. Main panel: GeoNet short-period and broadband seismographs (orange inverted triangles) used in this study for detection and picking, temporary seismographs (orange squares) used solely for picking, and continuous GNSS receivers (green triangles) active during the Kaikōura post-seismic period. Dashed lines mark the modeled subduction interface from C. A. Williams et al. (2013), and solid black lines mark faults of the NZ Active Fault Database (R. Langridge et al., 2016). Red lines mark the mapped surface ruptures of the Kaikōura earthquake (Clark et al., 2017), with fault names labeled. Inset: Regional setting of the Kaikōura region showing additional seismographs used for detection and location as inverted orange triangles. The location of the main panel is outlined as a red box, the region studied by Lanza et al. (2019) is shown as a blue box, and solid and dashed lines are the active fault database and modeled subduction interface respectively.

faults has a significant impact on where the inferred slip is concentrated (e.g., Hamling et al., 2017) and the propagation sequence from one fault to the next, exemplified by the different rupture pathways modeled by Ando and Kaneko (2018) and Ulrich et al. (2019). The implications of these models are wide ranging: from a general understanding of how earthquakes are able to propagate through complex fault systems, to more local implications for seismic hazard in central New Zealand.

Almost all published models of co-seismic and post-seismic deformation in the Kaikōura earthquake have been based on simplified fault models derived from near-surface geological data (e.g., Clark et al., 2017; Hamling et al., 2017; Holden et al., 2017; T. Wang et al., 2018; Xu et al., 2018). While these data provide essential controls, they do not provide robust information on the fault structure at depth, where most of the slip happens during earthquakes. Accurate earthquake catalogs provide a viable tool to constrain fault geometry at depth (e.g., Plesch et al., 2020), but have thus far been unavailable for the Kaikōura region, apart from the relatively small catalog developed by Lanza et al. (2019), and sparse moment tensor analysis by Cesca et al. (2017). Such catalogs of seismicity can also help illuminate other elements of the Kaikōura earthquake, including its relationship to prior seismicity in New Zealand, and how the various faults respond post-seismically.

1.1. Co-Seismic Kinematics and Rupture Propagation

Kinematic rupture models (Holden et al., 2017) show that the Kaikōura rupture started slowly on the Humps-Hundalee Fault system (Nicol et al., 2018; J. N. Williams et al., 2018). However, hypocenter estimates of the Kaikōura earthquake vary from being consistent with nucleation on the Humps Fault (Lanza et al., 2019; Nicol et al., 2018), to being as much as 7–15 km off the Humps Fault (according to the GeoNet (www.geonet.org.nz/earthquake/technical/2016p858000, last accessed April 24, 2021) and USGS solutions respectively (earthquake.usgs.gov/earthquakes/eventpage/us1000778i, last accessed April 24, 2021)).

Once initiated, the rupture propagated north-east towards the Hope Fault, but only produced a minor surface rupture (Hamling et al., 2017; Litchfield et al., 2018) of this fault, which previous paleoseismic studies have indicated to have a high Quaternary slip-rate (Litchfield et al., 2018). The rupture then stepped onto the Jordan Thrust-Kekerengu system where the maximum co-seismic surface offset of 11.8 m dextral occurred on the Kekerengu Fault (Kearse et al., 2018). The dominantly N-S-striking Papatea Fault, which intersects the junction between the Jordan Thrust and the Kekerengu Fault, also ruptured with up to 9.5 m of uplift and 6.1 m of sinistral motion (R. M. Langridge et al., 2018). Previous authors (e.g., Hamling et al., 2017; Holden et al., 2017) have noted that the high slip on the short (c. 19 km long) Papatea fault cannot be fit by elastic rupture models. The Papatea Fault intersects the Jordan Thrust-Kekerengu system at the point where dextral slip increases from the Jordan Thrust to the Kekerengu, and on-fault dip-slip motion changes sense, from normal on the Jordan Thrust to reverse on the Kekerengu (Kearse et al., 2018). This normal motion (NW down) on the Jordan Thrust appears not to be the dominant long-term sense of motion, with higher mountains on the NW side attesting to the dominantly oblique-reverse motion on the Jordan Thrust and Upper Kowhai Faults on geological timescales (Van Dissen & Yeats, 1991).

The details of the rupture pathway between the southern Humps-Hundalee fault system and the Kekerengu Fault are not well-resolved and two main pathways have been postulated. First, the offshore route, from the Hundalee Fault to the Papatea Fault via mostly unmapped offshore thrust faults. This trajectory appears consistent with a range of observations including off-fault damage at the Papatea-Jordan Thrust-Kekerengu junction (Klinger et al., 2018), kinematic (Holden et al., 2017) and dynamic rupture simulations (Ulrich et al., 2019), and tsunami modeling (Bai et al., 2017; Gusman et al., 2018). The second scenario involves rupture jumping from the Hundalee Fault to the Upper Kowhai Fault and onto the Jordan Thrust and Kekerengu Faults with limited slip on the intermediate Whites (Ando & Kaneko, 2018) and inferred Snowflake Spur Faults (Zinke et al., 2019). The lack of resolution of the fault network and possible inter-connections at depth inferred from surface observations alone mean that it remains unclear which scenario actually occurred.

The rupture continued to propagate northwards onto the Needles Fault and other faults in the Cape Campbell region before terminating near Cape Campbell itself (Kearse et al., 2018), in the region of the 2013 M_W 6.6 Cook Strait and Lake Grassmere earthquakes (Hamling et al., 2014). This northward rupture propagation resulted in strong shaking in New Zealand's capital city, Wellington (Bradley et al., 2017; Kaiser et al., 2017). The reasons for rupture terminating near Cape Campbell, despite the availability of faults straddling Cook Strait (Kearse et al., 2018), remains unclear. Dynamic rupture models (Ando & Kaneko, 2018; Ulrich et al., 2019) are able to capture most of the major features of the Kaikōura rupture, including the absence of slip on the Hope Fault, maximum co-seismic offset, and the termination near Cape Campbell. However,

how these two models achieve termination at Cape Campbell differs: Ando and Kaneko (2018) accounted for the termination by a c. 10° rotation in the prevailing stress field, which is indicated by focal mechanism inversions using data from prior to the Cook Strait earthquakes (Balfour et al., 2005; Townend et al., 2012). In contrast Ulrich et al. (2019) did not invoke a stress rotation, and instead artificially reduce the stress on the Needles Fault. It is also possible that the Cook Strait sequence invoked an as-yet unconstrained rotation in the stress field, resulting in the pre-Kaikōura stress field differing from that used by Ando and Kaneko (2018). Neither modeling study included the more favorably oriented faults that ruptured in the 2013 Cook Strait sequence.

In addition to the upper crustal faulting complexities, it remains unclear what role the underlying subduction interface played in the Kaikōura earthquake (Hamling, 2020). Lamb et al. (2018) suggested that the pattern of strain accumulation on the interface can explain the diversity of crustal faulting, but it is not clear that the interface played an active co-seismic role. Different models and data suggest differing contributions from the subduction interface to the co-seismic moment budget of the Kaikōura earthquake. Generally, models derived from regional data (e.g., Hamling et al., 2017; Gusman et al., 2018; Holden et al., 2017) require negligible seismic moment on the underlying interface. In contrast, studies using teleseismic data tend to favor more slip occurring on the subduction interface (e.g., T. Wang et al., 2018; Bai et al., 2017). Whether the subduction interface beneath the northern South Island can slip seismically is fundamentally important to understanding seismic hazard in this populous region of New Zealand (Wallace et al., 2018).

1.2. Post-Seismic Response

Afterslip inferred using geodetic data from the Kaikōura fault system for the months following the earthquake shows significant afterslip on the faults known to have ruptured (Mouslopoulou et al., 2019; Wallace et al., 2018) accompanied by afterslip or triggered slow-slip on the underlying subduction interface (Mouslopoulou et al., 2019; Wallace et al., 2017; Yu et al., 2020) and triggered slow-slip in other regions of the Hikurangi margin (Wallace et al., 2017). However, these models have used a relatively simple model of crustal faulting that does not capture the spatial extent of aftershocks, in part due to a lack of a dense, high-precision aftershock catalog.

Romanet and Ide (2019) observed tremor occurring prior to the Kaikōura earthquake, near the zone of mapped subduction interface afterslip, and suggested that the tremor may be related to interface slip. However, it is also possible that the tremor locates on the downdip extent of faults in the Marlborough Fault Zone. Further work is underway to better constrain these observations. Few aftershocks have yet been reliably linked to slip on the subduction interface (Lanza et al., 2019).

The Kaikōura earthquake generated a significant and ongoing aftershock sequence (Kaiser et al., 2017) and triggered earthquakes throughout New Zealand (Peng et al., 2018; Yao et al., 2021). However, it was relatively unproductive compared to average statistics for it's magnitude (Chamberlain et al., 2020; Christophersen et al., 2017) resulting in an over-estimation of aftershock rates early in the sequence when average aftershock behavior was used in forecasting (www.geonet.org.nz/earthquake/forecast/kaikoura, last accessed 22/01/2021). This relatively low-productivity aftershock sequence is in contrast to the similarly complex Ridgecrest earthquake, which was highly productive (Liu et al., 2019). Liu et al. (2019) suggested that the complexity of the Ridgecrest earthquake may have promoted productivity due to strong stress concentrations around fault step-overs. However, that explanation does not explain why the Kaikōura earthquake was relatively unproductive despite the involvement of significant stepovers and presumably associated stress concentrations.

1.3. Unresolved Questions

Most models of co- and post-seismic slip around the Kaikōura earthquake have used multi-fault models of fault ruptures, but these models have generally restricted the available faults to those with significant surface rupture, or simplifications thereof. The only study that we are aware of that used aftershocks to better define the rupture geometry focused on a small number of moment tensor solutions fixed at epicenters computed by GeoNet (Cesca et al., 2017). We demonstrate in this paper that these GeoNet locations are

poorly constrained due to the use of the IASP91 (Kennett & Engdahl, 1991) 1D velocity model (as also found by Lanza et al., 2019; Yao et al., 2021), rendering them too inaccurate for use in defining fault structures.

Previous analysis of Kaikōura aftershocks (Lanza et al., 2019) has demonstrated the diffuse nature of aftershocks around the step-over and Cape Campbell regions, which suggests slip occurred on additional crustal faults. In this paper we expand on this aftershock catalog to explore the diversity of faulting around the faults that ruptured in the Kaikōura earthquake, with the goal of shedding light on the pre-, co- and post-seismic faulting processes. We particularly focus on several fundamental aspects of the rupture that remain unresolved:

1. Rupture Initiation (Section 4.1): Where and how did the Kaikōura earthquake nucleate and were there observable precursory signals?
2. Rupture Pathway (Section 4.2): What was the likely rupture pathway between the southern fault system and the high-slip Kekerengu fault and how was this step-over accommodated kinematically?
3. Subduction Interface (Section 4.3): What was the seismogenic role of the subduction interface beneath the known crustal fault ruptures of the Kaikōura earthquake?
4. Termination (Section 4.4): Why did the rupture terminate at Cape Campbell and what was the significance of the previous 2013 M_W6.6 Cook Strait and Lake Grassmere earthquakes on this termination?
5. Post-seismic (Section 4.5): How did such co-seismic complexity affect post-seismic afterslip?

2. Data and Methods

To obtain a more detailed picture of the fault geometry at depth, and the pre- and post-seismic evolution of fault slip, we conducted a matched-filter search to generate a more complete representation of the seismicity. We analyzed >10 years of continuous data using earthquakes that occurred on the faults that ruptured co- and post-seismically in the Kaikōura earthquake as template events.

We used the catalog of 2,654 aftershocks and the mainshock picked and located by Lanza et al. (2019) as template events to provide a methodologically consistent set of phase-picks. This catalog includes every event of $M_L \geq 3$ cataloged by GeoNet that occurred between November 13 and May 13, 2017 (UTC) in a rectangular region between latitudes −43.00°and −40.80°and longitudes 172.75°and 175.20°, apart from 110 earthquakes that had poorly constrained depths. We previously attempted to use the GeoNet catalog directly to construct templates but found that the phase pick-quality was too variable, and the paucity of S-picks hindered our detection capability: the resulting catalog contained excessive false detections. The Lanza et al. (2019) catalog contains the dominant, moderate-to-large magnitude seismicity recorded in the seven months following the Kaikōura mainshock.

We constructed templates using data from 21 GeoNet broadband and short-period seismographs (Figure 1). We excluded strong-motion instruments from our analysis due to their variable timing quality (S. Bannister pers. comm.). Note that these stations were included in the analysis of Lanza et al. (2019) and may have degraded location quality in this prior work. We did not include temporary stations (e.g., from the STREWN network, as analyzed by Lanza et al. (2019)) in our detection effort to exclude bias in detections arising from variations in network geometry and station density.

Templates were made using EQcorrscan (Chamberlain et al., 2018). Continuous day-long data were detrended, resampled in the frequency domain to 30.0 Hz to reduce computational load, filtered using a 4th-order Butterworth bandpass filter between 1.5 and 12 Hz, and trimmed to 4 s length around the P and S phase-picks on the vertical and horizontal channels respectively. We tested a range of filters and template lengths and found that using a higher low-cut frequency resulted in additional false detections likely related to correlations with high-frequency noise, whereas using a lower low-cut frequency resulted in a degradation of correlations with true detections and an increase in background (e.g., noise) correlation sums. Increasing the length of templates resulted in excessive phase-overlap and compromised our ability to conduct later phase-picking analysis of detections. We removed channels with a signal-to-noise ratio less than four, where we computed signal-to-noise ratio using the ratio of the maximum amplitude in the template to the root-mean-squared amplitude of 100 s of pre-template noise. Finally we removed templates containing data from fewer than five stations, leaving a set of 2,584 templates.

We computed detections between January 1, 2009 and January 1, 2020 using the EQcorrscan package (Chamberlain et al., 2018) which computes the network-wide stack of the normalized cross-correlation between template waveforms and continuous data across multiple channels. We used the efficient FFTW (Fastest Fourier Transform in the West, Frigo and Johnson (1998)) backend that implements the chunked-correlation algorithm of Senobari et al. (2019), and the FMF (Fast-Matched-Filter, Beaucé et al. (2018)) GPU-based routine when a GPU was available. Note that in compiling this catalog we implemented full normalization in the FMF code to ensure compatibility with other correlations (Full-normalization in FMF implemented in pull request 38: github.com/beridel/fast_matched_filter/pull/38, last accessed July 29 2021).

Detections were made when the summed correlations exceeded 10× the median absolute deviation of the day-long stack of correlations, and had at least an average normalized correlation above 0.15. To cope with degraded correlations at the end of correlation epochs (in this case days) due to the delay-and-stack approach taken to compute the summed correlations, we overlapped each day of correlation by the maximum moveout in the templates. Detections from individual templates were required to be at least 4 s apart. To remove duplicate detections (e.g., detections of the same event by different templates), we retained only the detections with the highest average correlation if multiple detections occurred within 1 s of each other.

To enable location of the detected events and further remove false detections we computed cross-correlation derived phase-picks, following the methodology outlined by Warren-Smith et al. (2017). For each detection, the relevant channel of the template and continuous data were correlated in a short window of ±0.5 s around the assumed pick-time based on a time-shifted version of the template phase-pick. A pick was made at the maximum of this 1 s-long correlogram, if the maximum normalized correlation exceeded 0.4. Following this step, detections with picks on fewer than five stations were removed. This provided a catalog of 33,343 events comprising 899,460 phase-picks. In this picking step we incorporated the four temporary STREWN stations around Cape Campbell, and GeoNet station CRSZ, deployed after the Kaikōura earthquake, to enhance our locations without biasing our detections.

Because most of our detections were made during the active aftershock sequence of the Kaikōura earthquake, some of the correlation picks we made were associated with the wrong event due to overlapping events from different parts of the aftershock region. To combat this we undertook an additional quality-control step in which, for each event, we located the event using HYPOCENTER (Lienert & Havskov, 1995) and the 1D velocity model of Okada et al. (2019). If the root-mean-squared (RMS) travel-time residual of the location exceeded 1 s the pick with the highest residual was removed and the event located again. We repeated this process until either the RMS fell below 1 s, or picks from fewer than five stations remained. If the events RMS did not drop below 1 s with five or more stations, the event was discarded. This removed 30 events leaving us a total of 33,328 events and 896,727 phase picks.

We located the detected earthquakes using the NonLinLoc software of Lomax et al. (2000) and the New Zealand-wide 3D (NZ3D) velocity model of Eberhart-Phillips et al. (2017), version 2.2, which includes the updated tomography around the Cook Strait region conducted by Henrys et al. (2020). We note that the issues encountered by Lanza et al. (2019) in using NonLinLoc were rectified here by changing a flag in the NonLinLoc Grid2Time3D source-code. We also tested using SIMUL2014 (Eberhart-Phillips & Bannister, 2015) and found that the fit to the data was degraded compared to our NonLinLoc locations. We suspect that this reduced quality is because our events frequently contain S-picks without a corresponding P-pick, which SIMUL2014 cannot use. This is because S-phases usually correlate better than P-phases due to their high amplitudes. We were able to locate all events, but only 32,939 events are considered here because 389 occurred outside the study region (Figure 2).

Following this location step, we made automatic amplitude picks for all events and used these to compute local magnitudes. We used the EQcorrscan (Chamberlain et al., 2018) amplitude-picking routines which picks half the maximum peak-to-trough amplitude on a filtered, Wood-Anderson-simulated trace and corrects for the applied filter. Comparison of these automatic picks with GeoNet amplitude picks for similar events (both those within the template set and not in the template set) shows good agreement. We then computed local magnitudes by inverting for a local magnitude scale that maps to moment magnitude, following the methodology of (Michailos et al., 2019), taken from the moment tensor catalog maintained by

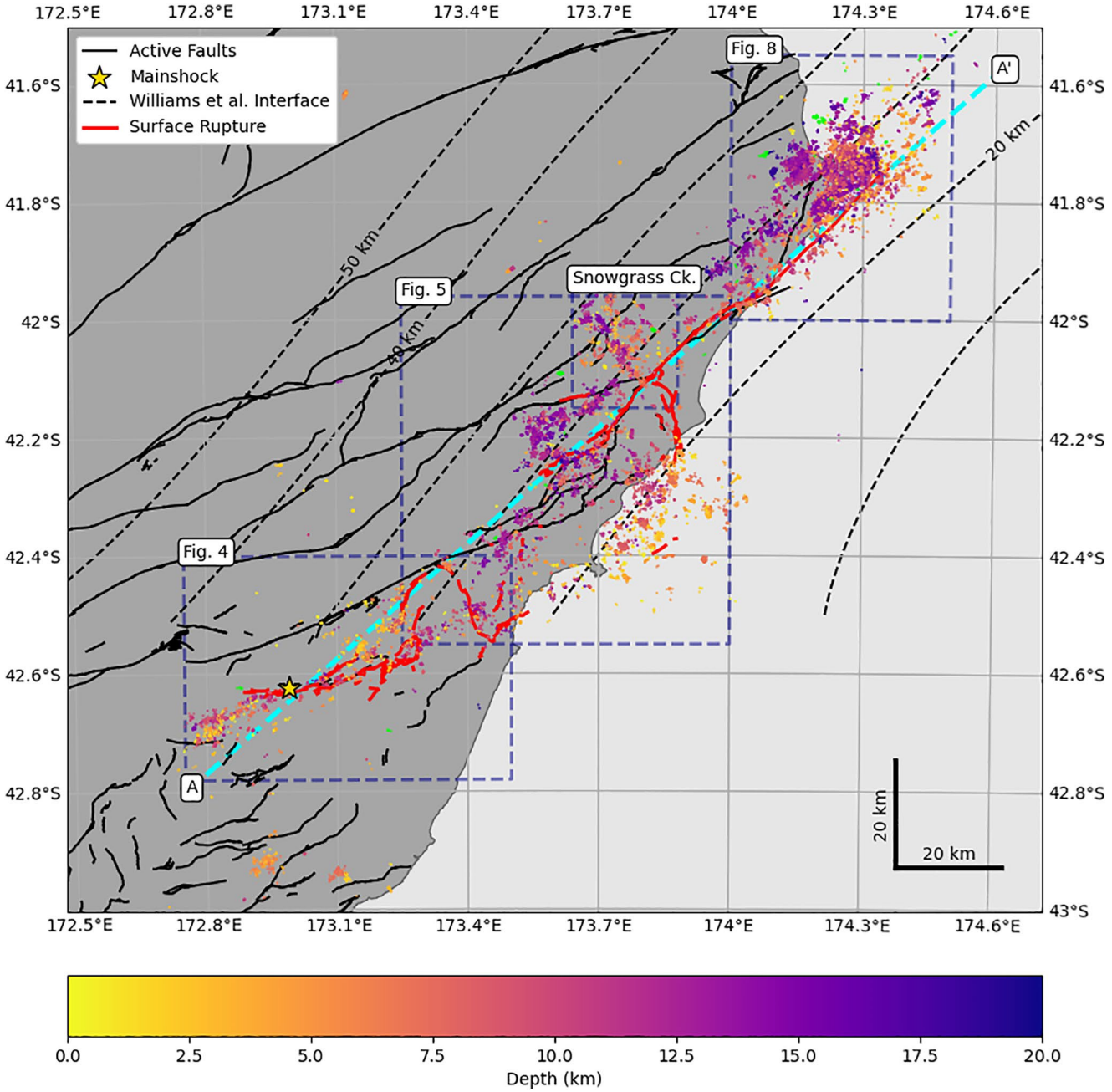

Figure 2. Earthquakes on and around the faults (red lines) that ruptured in the Kaikōura earthquake plotted as circles colored by depth. Earthquakes deeper than 20 km are plotted in green. Dashed contours mark the depth to the modeled subduction interface (C. A. Williams et al., 2013). The dashed cyan line, labeled A–A′ is the cross-section line shown in Figure 7. Dashed dark blue boxes mark the bounds of the relevant figures. The gold star marks the mainshock hypocenter computed here.

GeoNet (https://github.com/GeoNet/data/tree/main/moment-tensor, last accessed July 29 2021) and based on the work of Ristau (2013).

We subsequently undertook relative relocation of all earthquakes using the GrowClust software (Trugman & Shearer, 2017) and HypoDD (version 2.1b) (Waldhauser & Ellsworth, 2000). For GrowClust we used an average 1D velocity model extracted from the NZ3D velocity model (between 72–110 km in X and –100–80 km in Y in the coordinate system of Eberhart-Phillips and Bannister (2015), Table S1) used for initial location. For HypoDD we used the NZ3D model version 2.2 (Eberhart-Phillips & Bannister, 2015; Henrys

et al., 2020). We found little difference between the two location methods, and so report the GrowClust locations here because they provide robust, bootstrapped uncertainties (Trugman & Shearer, 2017). We were able to relocate 27,431 earthquakes in total.

Finally, we computed first-motion-derived focal mechanism solutions for template events. To compute template focal mechanisms we undertook manual polarity determination of the automatically determined P arrivals from Lanza et al. (2019). We included stations from the STREWN network, and strong-motion stations in the GeoNet network (station locations are plotted in Figure S8), but note that we did not use the timing of these phase arrivals in our location calculations. We then inverted for the best-fitting focal mechanisms of all template events with polarity picks at more than 8 stations ($n = 1{,}754$) using the Bayesian algorithm developed by Walsh et al. (2009). We used our NonLinLoc derived location estimates and uncertainties to compute takeoff angle and azimuth posterior density functions.

3. Results

We detected and located 33,328 earthquakes that occurred between January 1, 2009 and January 1, 2020 associated with the regions active during the aftershock sequence of the 2016 Kaikōura M7.8 earthquake. Of these earthquakes, we were able to compute precise relative relocations for a suite of 27,431 earthquakes (Figure 2). Our NonLinLoc locations have median 68% confidence uncertainties of between 1.8 km and 3.0 km (minimum and maximum confidence ellipsoid lengths) and 2.8 km in depth (Figure S6). Our GrowClust relocations have median relative uncertainties of 0.2 km in horizontal and depth directions.

As found by Lanza et al. (2019), but not by GeoNet, our hypocenter location for the Kaikōura mainshock (latitude –42.624, longitude 172.989, depth: 12.5 km) lies almost directly beneath the Humps Fault, about 8.2 km NNW from the GeoNet location (beyond the bounds of uncertainties of either location) and c. 2 km north of the location obtained by Nicol et al. (2018). We were not able to relocate the mainshock hypocenter (using Growclust or HypoDD) due to the complexity and clipping of the waveforms and resulting low correlations with other events. This mis-location by GeoNet is likely due to the use of an inappropriate velocity model (ISAP91: www.geonet.org.nz/earthquake/technical/2016p858000, last accessed September 7 2020). We discuss the variation in hypocenter location further in Section 4.1.

We obtain magnitudes ranging from 0.2–6.3 (Figure 3). We note that the maximum magnitude of 6.3 was computed for the M_W7.8 mainshock, which is beyond the range at which we would expect reliable amplitude-based local magnitudes (see Figure S5). The largest aftershock magnitude we calculated is M_L 5.9 30 minutes after the mainshock, for which GeoNet provide a magnitude of M_{Lv}6.2. In general our local magnitude scale gives lower magnitudes than GeoNet at high magnitudes (Figure S5). We were unable to calculate magnitudes for 50 earthquakes due to insufficient amplitude picks of sufficient quality. The completeness of our catalog is strongly variable in time: as noted by Hainzl (2016), during periods of high-rate seismicity the magnitude of completeness increases, and we observe this after the Kaikōura mainshock. Before and within a few months after the mainshock, our magnitude of completeness is around M_L1.2, however in the hours after the mainshock the completeness becomes as elevated as M_L3.8 (Figure 3). One of the main causes of elevated completeness, despite the ability of the matched-filter method to detect earthquakes with overlapping waveforms, is the restriction in our workflow to only detect events separated by at least 1 s.

The vast majority of earthquakes in our catalog are aftershocks of the Kaikōura earthquake (30,652 events, or 92%, occurred after the mainshock). The earliest aftershock we detect occurred 2 minutes and 48 s after the mainshock origin time, approximately 45–65 s after the completion of the mainshock rupture (Holden et al., 2017). However our catalog also includes aftershocks of the Cook Strait earthquakes, with 2,326 earthquakes between the start of the Cook Strait sequence on the 18th of July 2013 and the Kaikōura mainshock. Some events in our catalog appear to be associated with failure within the subducted plate. The sequence of earthquakes visible in Figure 3 at c. 125 km along the section occur at c. 25 km depth and have focal mechanisms consistent with normal-faulting in the subducted slab. Interestingly this family of earthquakes culminated in a sequence of eight earthquakes in the seven days prior to the Kaikōura mainshock. We also detect limited earthquakes associated with slip on the subduction interface made by templates representing

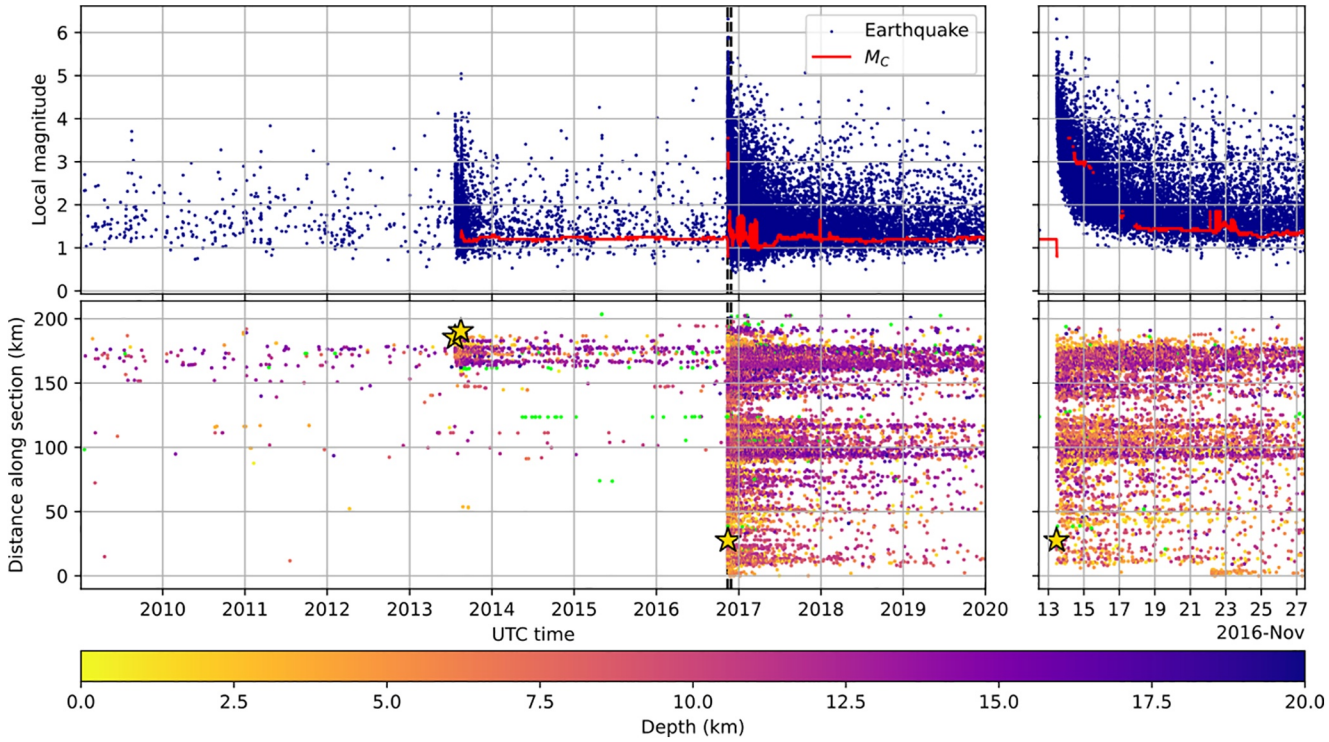

Figure 3. Upper panel: Local magnitudes for all earthquakes in our catalog (blue) and magnitude of completeness computed by goodness-of-fit (Wiemer et al., 2000) (red). Magnitude of completeness was computed using a sliding window of 1,000 events. Magnitude of completeness is only shown when at-least 300 magnitudes were above the best fitting completeness, and the fit was above 98%. Lower panel: Earthquakes projected onto the A–A′ cross-section (Figure 2), and plotted against origin-time. Earthquakes are colored by depth. Earthquakes deeper than 20 km are plotted in green and the gray ellipse outlines the deep normal-faulting sequence discussed in the text. The Lake Grassmere, Cook Strait and Kaikōura earthquakes are plotted as gold stars. Right panels show zoomed in views of the two weeks following the Kaikōura mainshock, marked as vertical dashed black lines in the left panels.

likely interface events reported by Lanza et al. (2019) near Cape Campbell. Most (28,768 or 86% or absolute locations and of 24,568 or 90% relative relocations) of our earthquakes are found to have been shallower than 15 km.

4. Discussion

This updated and expanded catalog of earthquakes on and surrounding the faults that ruptured in the Kaikōura earthquake serves as the basis to re-evaluate some of the outstanding questions regarding this complex earthquake. Here we discuss the key questions outlined previously and highlight some key fault structures that have previously been poorly resolved or unknown.

4.1. Rupture Initiation

Multiple hypocenter locations for the Kaikōura earthquake are now available and, as demonstrated by Nicol et al. (2018), there is some inconsistency between them. In our locations we find that the mainshock hypocenter locates almost directly beneath the surface trace of the Humps Fault, at a depth of 12.5 ± 5.8 km (Figure 4). The first-motion-derived focal mechanism of the mainshock that we construct here (strike/dip/rake of 245°/80°/175°) is consistent with dextral slip on a steeply dipping plane similar to the strike of the Humps Fault. A Gaussian fit to the NonLinLoc uncertainties at the 1σ level provides a horizontal uncertainty ellipse oriented at 96° with a maximum length of 2.3 km and minimum length of 1.8 km. Our location is slightly different (but within uncertainty) from that of the previous solution of Lanza et al. (2019), whose phase picks we use here, and notably different from the Geonet location that does not place the hypocenter on the Humps Fault. The GeoNet hypocenter could indicate that an initial rupture on a separate fault to the south occurred, which subsequently triggered slip on the Humps Fault as suggested by Ando and Kaneko (2018)

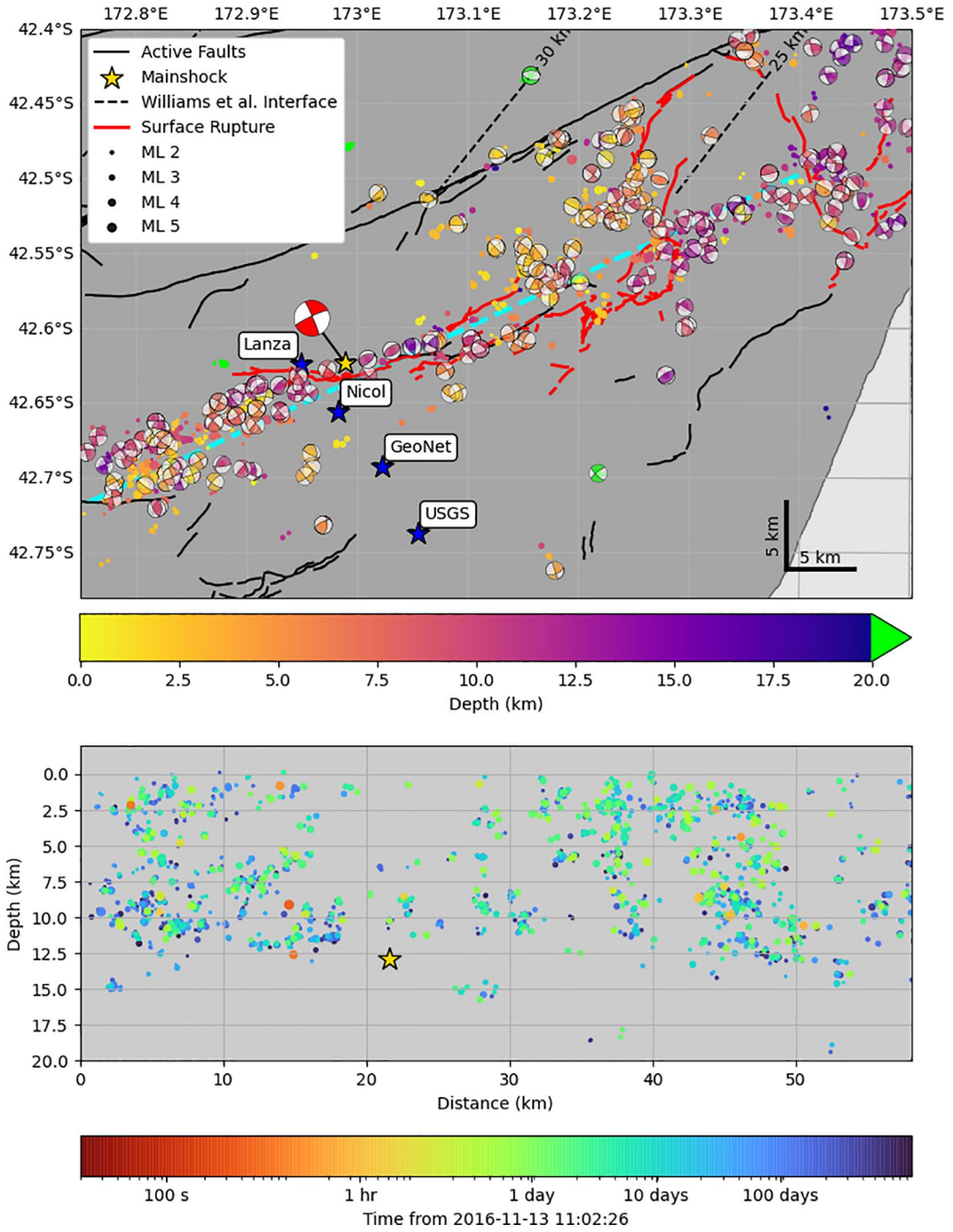

Figure 4. Nucleation region of the Kaikōura earthquake. Upper panel: map of relocated earthquakes (circles colored by depth and scaled by magnitude) and focal mechanisms of template events, colored by depth. Earthquakes deeper than 20 km are plotted in green. Mainshock location is marked by a star: note that this is an absolute location rather than a relocation for reasons explained in the text. The first-motion derived focal mechanism of the mainshock is shown in red. Alternative mainshock locations are plotted as blue stars and labeled as Lanza, Nicol, GeoNet and USGS for the Lanza et al. (2019), Nicol et al. (2018) GeoNet and USGS solutions respectively. Mapped surface ruptures are plotted as red lines, and other faults of the NZ active faults database are plotted in black. Dashed black contours mark the modeled subduction interface from C. A. Williams et al. (2013). The dashed cyan line shows the cross-section line plotted in the lower panel. Lower panel: Cross-section (SW to NE) of relocated hypocenters projected onto the cyan line in the upper panel. Earthquakes are colored by time since 30 s prior to mainshock, note that the colorscale is logarithmic. Earthquakes are scaled by magnitude. The star marks the absolute location of the mainshock.

to explain some of the mismatch in the initial rupture speed between their model and observations. However, we are confident that the rupture did in fact nucleate on the Humps Fault, and discuss possible causes of the discrepancies in locations below.

In this work we have not used picks on the strong-motion sites with known timing problems. We also use an updated velocity model, and a different location method compared to Lanza et al. (2019). When we use the same location method (using the software SIMUL) and/or use the same velocity model as Lanza et al. (2019), we obtain a similar result to our preferred solution, suggesting that the main source of error in the previous location of Lanza et al. (2019) was from the inclusion of picks from sites with problematic timing.

The GeoNet preferred location for the mainshock hypocenter (at the time of writing this, April 24, 2021, was at −42.693°N, 173.022°E and 15.11 km depth) lies 8.2 km to the south of our location, beyond the combined uncertainties in our location and the quoted horizontal uncertainty in the GeoNet location (2.3 km in latitude and 3.4 km in longitude). The GeoNet solution is computed using the IASP91 (Kennett & Engdahl, 1991) global 1D velocity model and the LOCSAT location program (Bratt & Nagy, 1991). When we locate the mainshock using the GeoNet pick times in NonLinLoc using the NZ3D 2.2 velocity model used here we obtain a similar location to our location (within uncertainty). We suggest that the use of the global 1D velocity model is inappropriate for accurate location of crustal seismicity in New Zealand, and results in incorrect locations and under estimated location uncertainties, as also shown in central North Island by Illsley-Kemp et al. (2021). Similar issues are likely to apply to other location solutions for the Kaikōura mainshock that do not use an appropriate velocity model.

The location computed by Nicol et al. (2018) is within the uncertainty of our location, and was computed using a similar method to that used here. However, the aftershock relocations computed by Nicol et al. (2018) use GeoNet locations as starting locations, which are inaccurate due to the use of the IASP91 velocity model. As such, relocation from these inaccurate starting locations is the likely cause of difference between the relocations of Nicol et al. (2018) and those presented here, which here delineate a nearly vertical structure consistent with our mainshock focal mechanism. The south-dipping lineation extending through the subduction interface shown by Nicol et al. (2018) is not visible in our relocations, probably due to more robust starting locations used here.

We note that a foreshock c. 7 s prior to the mainshock (Figure S1) may also have contributed to inaccuracies in mainshock location: if picks were made on the much smaller foreshock P-phases for the four GeoNet stations that they are visible on then these arrival times would bias the location. This foreshock is located close to the mainshock, but the mainshock obscures the S-phase on most stations and the P-phase is only visible on four stations due to the size of the foreshock, and the resulting location we obtain has high uncertainties. We did not detect this foreshock with our matched-filter detector due to the poor signal on most stations, and it is therefore not included in our catalog.

In summary, our more accurate mainshock location and focal mechanism confirm that the Kaikōura earthquake most likely nucleated as a dextral strike-slip rupture of the Humps Fault, and confirm that the Humps Fault here is steeply dipping (c. 80°) to the North. This suggests that off-fault triggering did not play a strong role in the nucleation of the Kaikōura earthquake, and other factors must be the cause of the early long-duration release of seismic energy. Ulrich et al. (2019) were able to reproduce the slow initial phase of the rupture through the Humps-Hundalee system in their dynamic rupture simulation. Finally, it is worth noting that any seismic backprojections that compute the location of high-frequency radiation sources relative to the mainshock may be biased by the use of inaccurate hypocenters (e.g., Tan et al., 2019; D. Wang et al., 2018).

We do not observe precursory seismicity in our catalog aside from the foreshock approximately 7 s prior to the mainshock which we did not detect by matched-filter and is not included in our final catalog. This includes no seismicity in the epicentral region following any of the 2010 Darfield earthquake, 2011 Christchurch earthquakes, or the 2013 Cook Strait sequence, which are likely to have induced dynamic stress changes in the epicentral region of the Kaikōura earthquake. We attempted to run a focused matched-filter search using GeoNet data and the 7 s foreshock as a template, but this did not make any further reliable detections.

We note that our catalog is likely biased by being constructed using only aftershocks as templates, and the presence of at least one visible foreshock should motivate further analysis of foreshock activity here.

4.2. Rupture Pathway

The Kaikōura earthquake involved substantial rupture (>1.5 m surface slip) of at least 13 faults (Litchfield et al., 2018). Initial observations suggested that large stepovers (up to 20 km), particularly between the southern faults (Humps-Hundalee system) and the high slip Kekerengu Fault, were present (Hamling et al., 2017; Kaiser et al., 2017). Such large stepovers commonly correspond to rupture termination points (Harris et al., 1991; Wesnousky, 2006). More recently, additional faults, including the Point Keen or other offshore reverse faults, and/or links between the Hundalee and Jordan Thrust/Upper Kowhai Faults (via the Leader and Whites Faults) have been postulated to explain the rupture sequence (e.g., Ando & Kaneko, 2018; Zinke et al., 2019). In particular, the dynamic rupture model of Ando and Kaneko (2018) has rupture propagating from the Hundalee Fault to the Upper Kowhai and Jordan Thrust Faults with limited slip on the linking Whites Fault (Figure 6), and suggests that this step-over was accommodated mostly by transient dynamic stresses or elastic waves. In contrast, the dynamic rupture model of Ulrich et al. (2019) has rupture propagating from the Hundalee Fault onto the offshore reverse faults before triggering slip on the Papatea Fault, which then caused rupture of the Jordan Thrust and Kekerengu Faults.

Although we do not have direct co-seismic evidence in our catalog of the rupture pathway, our earthquake locations help to illuminate the structure of these linking faults at depth (Figure 5). Two key faults emerge: (a) an offshore, dominantly reverse, structure similar to the Point Keen Fault modeled by Ulrich et al. (2019); Hamling et al. (2017) and (b) a previously unidentified strike-slip, near-vertical structure linking the Papatea-Jordan Thrust-Kekerengu-Fidget junction to the inland, unruptured Clarence Fault. We herein refer to this second new fault as the Snowgrass Creek Fault, named after a nearby stream. The Snowgrass Creek Fault strikes approximately 140°, has a near vertical dip, and a surface length of approximately 12 km. Note that this fault is not associated with any reported surface rupture. There is also a continuous trend of earthquake locations spanning the gap between the southern fault system and the Jordan Thrust, suggesting that either the offshore route, via the offshore thrust system, or the onshore route, via the Whites Fault are viable options for rupture propagation.

Several key observations provide further constraints on the most likely rupture route for the Kaikōura earthquake, principally the occurrence of a small, localized tsunami (Gusman et al., 2018), and the inverted motion of the Jordan Thrust, which hosted normal motion rather than the reverse motion, as would be expected from the geological record (Howell et al., 2020; Van Dissen & Yeats, 1991). We propose that these two factors, alongside our observation that offshore thrust faulting spans the gap between the Hundalee Fault and the Papatea Fault, require that the earthquake propagated via the offshore route (Figure 6). In addition the observation of a tsunami requires some co-seismic offshore deformation which would be provided by offshore thrust faulting (Gusman et al., 2018), and the normal (inverted) sense of slip on the Jordan Thrust Fault can be explained by our preferred model. This is in agreement with recent modeling studies by Ulrich et al. (2019) and Klinger et al. (2018).

In our preferred rupture scenario we suggest that the offshore thrust fault (or faults, here labeled as the Point Keen Fault for consistency, despite the opposite sense of slip compared to the geologically recognised Point Keen Fault (Litchfield et al., 2018)), the Papatea Fault, and extending into the newly discovered Snowgrass Creek Fault acted as one thrust block with a sinistral north-western edge (Figure 6). Within this thrust block, the normal motion of the usually reverse Jordan Thrust Fault occurs as a consequence of the eastward motion of eastern side of the block (normally the footwall). In other words, the coastal side of the Jordan Thrust is extended seawards relative to the pinned inland side resulting in normal motion.

This scenario can also help to explain the high slip on the Papatea Fault. In this scenario, the Papatea Fault sits at the corner between dominantly thrust motion offshore, to dominantly sinistral-normal oblique motion onshore on the Snowgrass Creek Fault. Not only does this scenario provide additional fault length for the combined Papatea-Snowgrass Creek-Point Keen Fault system, meaning that co-seismic displacements scale more consistently with fault length, but also that the Papatea Fault acts in a similar style to a restraining

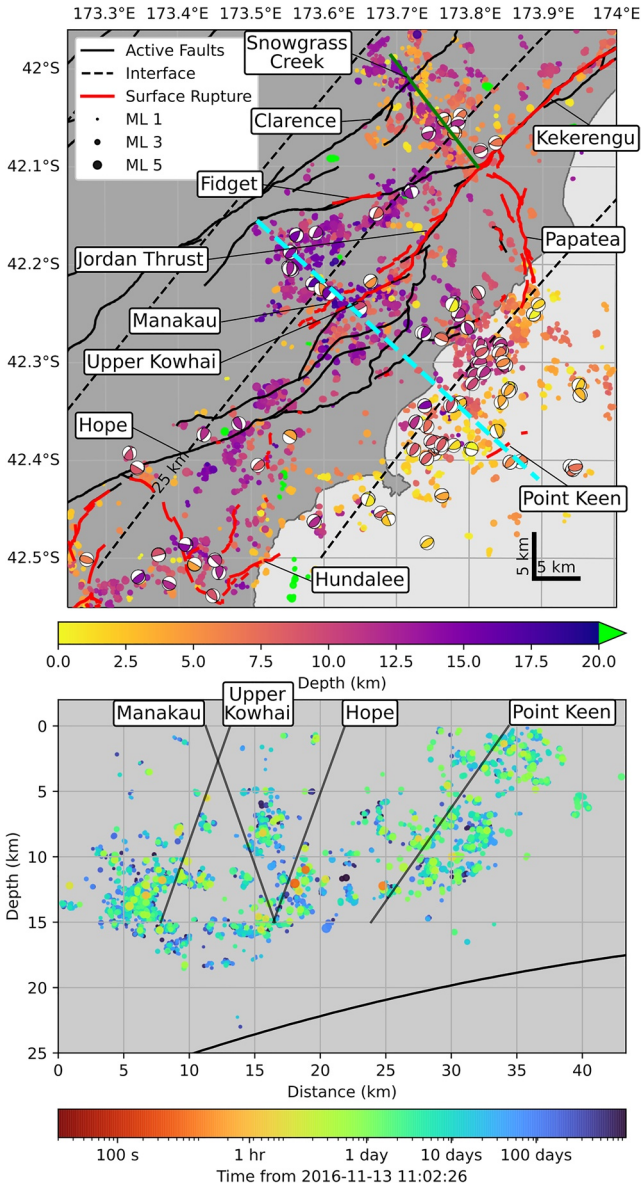

Figure 5. Earthquake locations around the transition from southern/epicentral faults to the Kekerengu fault. Top: map view of relocated earthquakes plotted as circles colored by depth and scaled by magnitude. Earthquakes deeper than 20 km are plotted in green. Thrust focal mechanisms (45°<rake<135°) for template events are also plotted, colored by depth. Active faults are plotted in black, and faults with known surface rupture during the Kaikōura earthquake are plotted in red. Black dashed contours mark the depth to the interface model of C. A. Williams et al. (2013). The cyan dashed line marks the cross-section line shown in the lower panel. The green solid line marks the inferred location of the newly identified Snowgrass Creek fault (labeled). Note that the surface dip of the Clarence Fault is c. 70°NW (Rattenbury & Isaac, 2012), and the Snowgrass Creek fault appears to terminate at the Clarence Fault at depth. Bottom: Cross-section perpendicular to the dominant strike of reverse focal mechanisms. Earthquakes within 7.5 km of the cross-section are projected onto the line. Solid straight lines mark the locations and dips of cross-section intersecting faults from Litchfield et al. (2018). The solid curved line at depth marks the subduction interface model of C. A. Williams et al. (2013). Note that the broad cluster of earthquakes at the down-dip end of the Upper Kowhai Fault is likely associated with projecting earthquakes on a fault striking obliquely to the cross-section. Similarly, our preferred arcuate geometry of offshore thrusting, and variable dip provides an explanation for the broad region of earthquakes below the inferred Point Keen Fault.

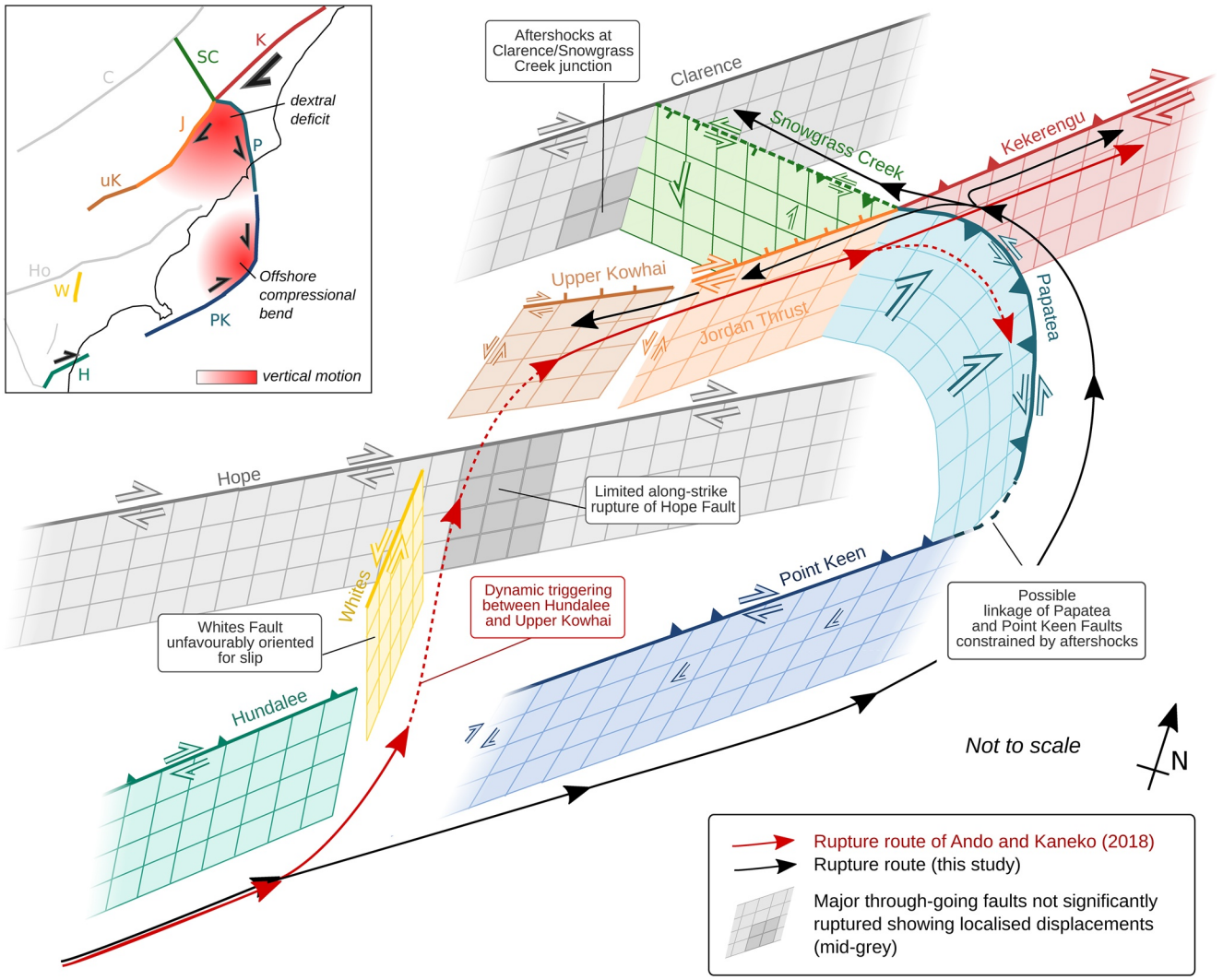

Figure 6. Schematic, not-to scale cartoon illustrating links between faults in the stepover region between the southern faults and the high slip Kekerengu Fault, and how the Papatea Fault may operate as a restraining pop-up. Faults in gray represent major through-going structures of the Marlborough Fault Zone (the Hope and Clarence Faults) which did not have significant co-seismic rupture, but which may have localized slip at depth near fault junctions as indicated by darker gray shading. Note that the Hope Fault is truncated for visibility, but extends further offshore than plotted. Colored, outlined arrows on faults show sense of co-seismic motion, approximately scaled by size to show relative slip magnitudes between different faults. The thin red line with arrows shows preferred inland rupture route of Ando and Kaneko (2018) via the Whites Fault (inferred, dashed line) and triggered slip on the Papatea (also denoted by dashed line). The thin black line with arrows shows our preferred offshore rupture route, with bi-lateral rupture originating from the Papatea-Kekerengu-Snowgrass Creek-Jordan Thrust junction. Inset shows simplified map view of faults, colored as in main plot, illustrating how the Papatea-Point Keen connection forms an offshore compressional bend with anticipated vertical motion.

bend, for example, with large co-seismic strain exceeding the long-term accumulated elastic strain, which other authors have suggested is insufficient to explain the slip amplitude on the Papatea Fault (e.g., Diederichs et al., 2019).

We use the same equations, converted to SI units, as R. M. Langridge et al. (2018), after Stirling et al. (2012), namely:

$$M_W = 2/3 \log W + 4/3 \log L - 1.82, \quad (1)$$

where W is fault width and L is fault length, both in meters, and

$$M_0 = \mu LWD, \quad (2)$$

where M_0 is the seismic moment in N·m, μ is the shear modulus, which Stirling et al. (2012) assume to be 3×10^{10} Pa, L and W are as before, and D is the single-event displacement in meters. M_0 is calculated using:

$$\log M_0 = 9.05 + 1.5 M_W. \quad (3)$$

This way, we are able to estimate single-event displacements for various fault combinations. We deduce that R. M. Langridge et al. (2018) adopted a fault width of 18.5 km based on the magnitude they compute. Using this fault width and a combination of the Papatea and Snowgrass Creek faults (which adds approximately 15 km to the length when incorporating the dip of the Clarence Fault and hence additional length of the Snowgrass Creek Fault at depth) we find a single-event displacement of 2.3 m. Incorporating the Point Keen Fault in our preferred geometry results in an 83 km total length and average displacement of 5.8 m. Finally, including the section of the Hundalee Fault between the coast and the Stone Jug Fault increases the length to 93 km and slip to 6.5 m. The average net slip on the Papatea Fault was measured to be 6.4 ± 0.2 (R. M. Langridge et al., 2018), reinforcing our proposed combined fault system explanation.

The existence of the Snowgrass Creek Fault also helps to explain the drop in slip across the Kekerengu-Jordan Thrust junction, despite the similar strikes of these two faults. A simple model of this junction is that of a quadruple junction between the Jordan Thrust, Papatea, Kekerengu and Snowgrass Creek Faults (discounting the Fidget Fault that has mapped surface rupture away from the junction, but not nearby (Litchfield et al., 2018)). By averaging the InSAR derived coseismic displacement field (Hamling, 2020) in blocks around the fault system (see Figures S2 and S3) we estimate the strike-parallel and perpendicular components of motion on the Snowgrass Creek to be 1.3 m sinistral and 3.4 m of extension. The resulting sinistral transtensional motion is consistent with the dominant aftershock focal mechanisms (Figure S8). The strong change in the InSAR-derived North-South displacement field aligns with the strike of the Snowgrass Creek Fault constrained by our earthquake locations.

Including the Snowgrass Creek Fault as a separation between the western side of the Kekerengu Fault and the western (inland) side of the Jordan Thrust reduces the required dextral motion from 6.2 m on the Kekerengu to 3.3 m on the Jordan Thrust. The difference in these estimated offsets corresponds well with the difference in dextral offsets measured by Kearse et al. (2018), which rise from c. 1–8 m on the Jordan Thrust, and are generally between 10–12 m on the Kekerengu Fault (see Figures S2 and S3). Without the Snowgrass Creek Fault, block offsets require 5.1 and 5.0 m of dextral offset on the Kekerengu and Jordan Thrust Faults, which does not allow for change in the change in dextral offset observed. Our estimates do not capture the total slip on the faults because we use spatially averaged displacements in off-fault blocks to capture the general kinematics. Nevertheless, the change in slip between the Kekerengu and Jordan Thrust cannot be accommodated without some additional deformation, and the Snowgrass Creek Fault provides a viable structure for this deformation.

We suggest, therefore, that the Kaikōura earthquake propagated from the Hundalee Fault onto the offshore thrust system, which then activated the Papatea and Snowgrass Creek Faults, which in turn triggered slip on the Kekerengu Fault. In this model, the role of the Jordan Thrust is minor, and the extension of aftershocks between the Jordan Thrust to the Whites Fault is a consequence of the underlying thrust system. This scenario agrees with the dynamic rupture simulation of Ulrich et al. (2019), but is at odds with that of Ando and Kaneko (2018) whose model did not result in significant slip on the Papatea Fault. We note that both Ando and Kaneko (2018) and Ulrich et al. (2019) have used a shallower dip on the offshore thrust system than the 45–60° dip found here, which results in a reduced possible stress-drop in the model of Ando and Kaneko (2018), making it a less favorable rupture pathway in their model.

The Snowgrass Creek Fault also appears to link with the Clarence Fault, a key component of the Marlborough Fault system (Van Dissen & Nicol, 2009) that did not rupture in the Kaikōura earthquake. One of the earliest aftershocks we detected, a M_L4.8 within nine minutes of the mainshock origin time, occurred at the junction of the Snowgrass Creek and Clarence Faults, suggesting that the Clarence Fault may have been active early in the aftershock sequence. That neither the Hope nor the Clarence Faults had significant co-seismic rupture despite evident triggered aftershocks, remains an intriguing observation.

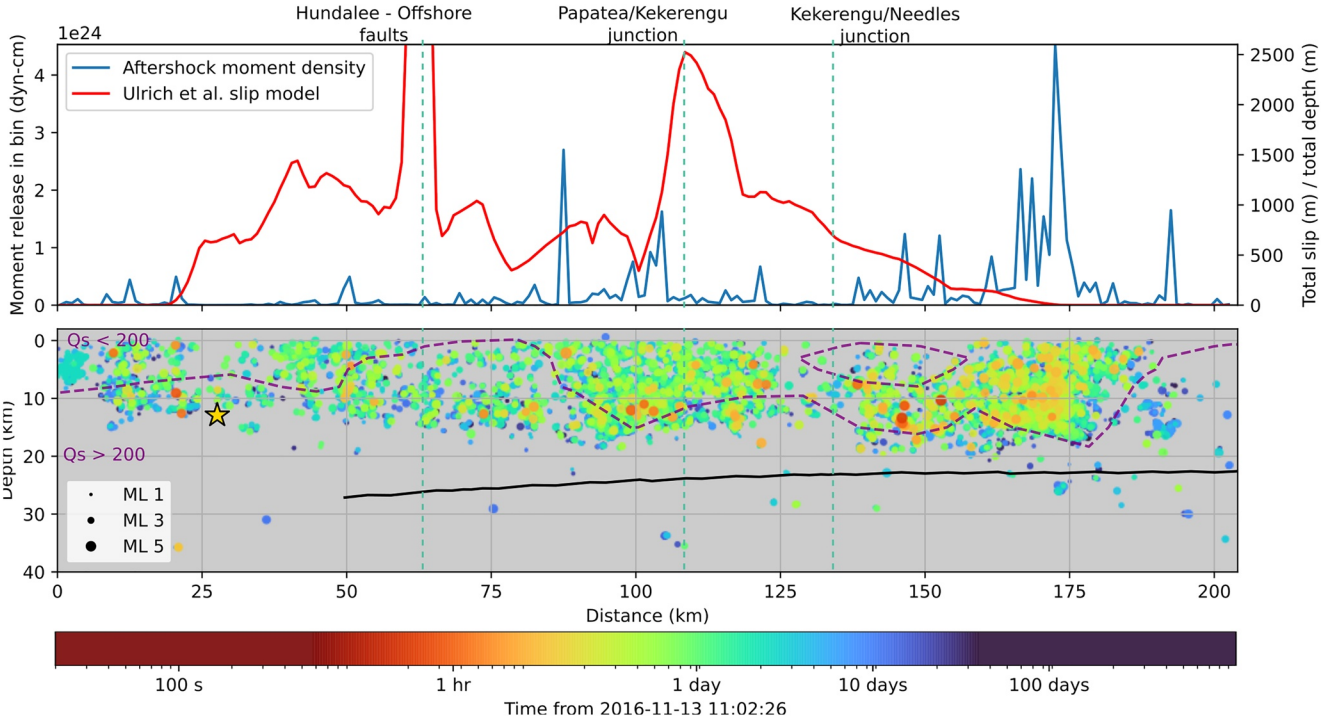

Figure 7. Along-strike earthquake distribution, along line A–A′ shown on Figure 2. Top: Aftershock moment density (blue) computed in 1 km bins perpendicular to the cross-section, and slip density derived by Ulrich et al. (2019) (red). Note that the projection of all slip in this 3D fault geometry onto a single plane results in the summation of slip across multiple fault strands. The peak in slip around 65 km along the section occurs at the corner between the Stone Jug and Hundalee faults and is likely unrealistic, and in part due to the projection of slip on a single plane. Bottom: Aftershock locations colored by time since 30 s prior to the the Kaikōura mainshock. Note that the color-scale is logarithmic. The location of the epicenter of the mainshock is shown by a gold star, and the depth of the interface from C. A. Williams et al. (2013) is shown as a solid line. The purple dashed contour marks the $Qs = 200$ contour from the NZW3D 2.2 model (Henrys et al., 2020).

4.3. Subduction Interface

We observe no earthquakes consistent with slip on the subduction interface beneath the majority of the upper-plate faults (Figure 7). The few earthquakes observed close to the subduction interface (e.g., at 23 km depth in Figure 5) show normal-faulting mechanisms, consistent with extension in the down-going plate, and were active prior to the Kaikōura earthquake. Some earthquakes consistent with subduction interface slip occur beneath the Cape Campbell region, as shown by Lanza et al. (2019) and here (Figure 8), but not all show mechanisms consistent with interface slip here. It may be that the northern-tip of South Island is the point where the subduction interface becomes seismically active, as proposed by Henrys et al. (2020).

When considering the significance of a lack of aftershocks in our catalog on the subduction interface it is important to restate the limitations of matched-filter catalogs. Such catalogs by definition only contain earthquakes similar to those in the template data set: if we do not have any subduction interface earthquakes in our template set then we should not be surprised to see no subduction related events in the final catalog. However, our template catalog is composed of all earthquakes in the GeoNet catalog between November 13, 2016 and May 12, 2017 larger than M_L3 (Lanza et al., 2019). As such, any missing seismicity should be of small magnitude and therefore likely contributed minimally to the total (post-seismic) moment release.

Our data set provides no direct constraints on whether the subduction interface slipped co-seismically, but by more accurately mapping crustal seismicity we are able to robustly demonstrate the existence of offshore thrust faulting south of the Kekerengu Fault. Such offshore faulting has been previously used in models that recreate co-seismic data without the need for significant slip on a subduction source (e.g., Clark et al., 2017; Gusman et al., 2018). Incorporating more realistic models of crustal faulting at depth, derived from our catalog, may provide greater constraints on the co-seismic role of the subduction interface.

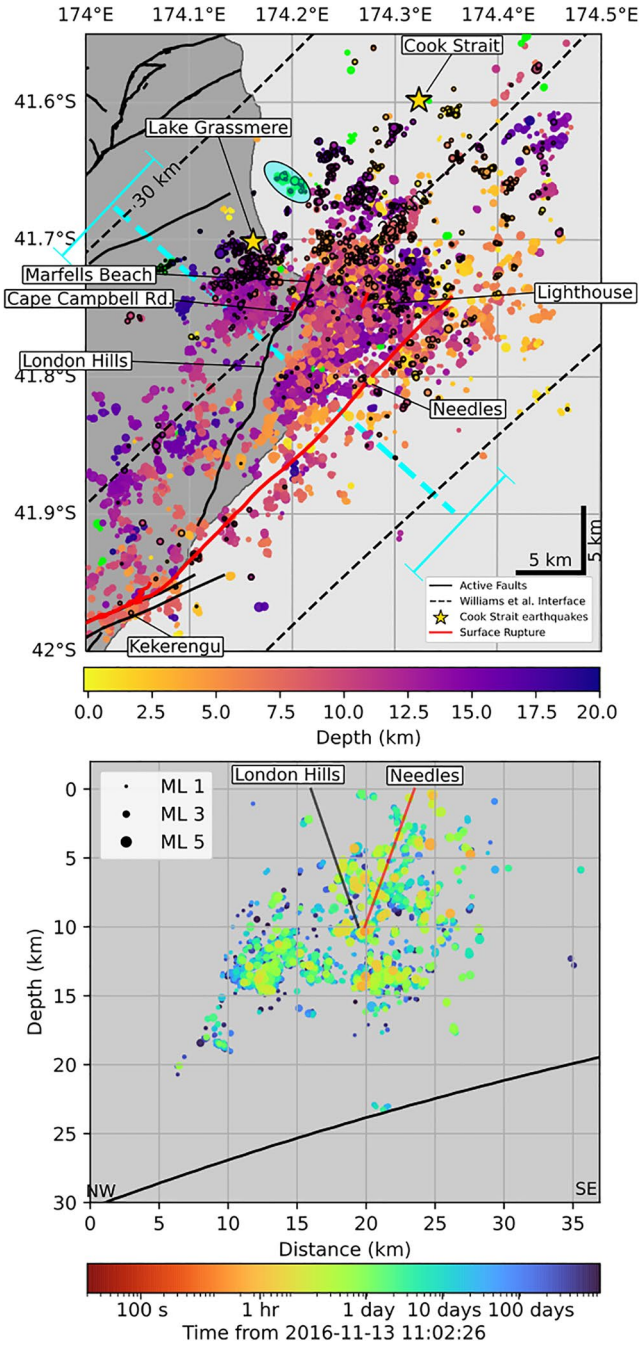

Figure 8. Earthquake locations near the termination of the Kaikōura earthquake. Top: Map view of earthquake relocations colored by depth. Earthquakes deeper than 20 km are colored green. Earthquakes with black outlines mark events that occurred prior to the Kaikōura mainshock, including events triggered by the Cook Strait and Lake Grassmere earthquakes in 2013, which are plotted as gold stars. Active faults without surface rupture from the Kaikōura earthquake are plotted as black lines, and those with surface rupture are plotted in red. Black dashed contours show the model of the Hikurangi subduction interface from C. A. Williams et al. (2013). The teal oval outlines the events close to the subduction interface that have mechanisms possibly related to slip on the interface as identified by Lanza et al. (2019). The dashed cyan line marks the cross-section plotted below, and the width of the swath (10 km) is shown at each end of the cross-section line. Bottom: Cross-section of earthquake locations colored by time after 30 s prior to the Kaikōura mainshock within 5 km of the cross-section line. The subduction interface is shown as a curved solid black line, and the projections of the Needles (surface dip of 70°, (Litchfield et al., 2018)) and London Hills (surface dip of 70°(R. Langridge et al., 2016)) faults to 10 km depth are shown.

The lack of aftershocks on the subduction interface does not preclude afterslip on the interface because this afterslip could be aseismic. However, it seems unlikely that if the subduction interface is aseismic in the post-seismic period that it would have contributed significantly to the co-seismic seismic wavefield. The published models of post-seismic slip have used simple models of crustal faulting (for instance Wallace et al. (2018) use four crustal fault sources attempting to simulate the Humps, Kekerengu/Jordan Thrust, Needles and an offshore thrust fault). The simplicity in crustal faults may lead to inaccurate mapping of slip onto the underlying subduction interface.

For example, in the Cape Campbell area, at the northern tip of South Island, strong co- and post-seismic uplift occurred (Wallace et al., 2018). This uplift includes a large short-wavelength component: the uplift at GNSS station CMBL is more than triple that at station WITH (Figures 1 and 9), within a few tens of kilometers. WITH and CMBL are separated by the faults that ruptured in the Lake Grassmere earthquake (Hamling et al., 2014), which were re-invigorated during the Kaikōura aftershock sequence (Figure 8). These faults are more shallowly dipping than the Needles Fault, and have a significant reverse component (Hamling et al., 2014), but the pattern of uplift observed in the Kaikōura earthquake is the reverse of that in the Lake Grassmere earthquake (Hamling et al., 2014). This suggests that either the Lake Grassmere and Cook Strait Faults were reactivated with a normal sense of motion (but we do not observe normal focal mechanisms in this region), or other reverse faults dipping to the East, such as the London Hills Fault, were responsible for this short-wavelength uplift. No faults between WITH and CMBL with this sense of motion were included in the afterslip model of Wallace et al. (2018). Inclusion of these faults, which have a strong aftershock signature (Figure 8) may reduce the need for interface slip beneath Cape Campbell.

Incorporating more realistic and complex crustal faulting is unlikely to completely remove the need for slip on the underlying subduction interface: crustal faults are likely to help to explain short-wavelength geodetic features, but not the long-wavelength features seen in both the post-seismic InSAR and GNSS data (Wallace et al., 2018).

Recent modeling work by Eberhart-Phillips et al. (2021), constrained by seismic attenuation modeling results, shows that deformation between the subducted Pacific plate and overlying Australian plate is likely to be ductile with no clear interface structure. In this scenario, ductile deformation rather than interface slip may be controlling the long-wavelength post-seismic signature. Such ductile deformation would likely be aseismic, consistent with both the geodetic signature and the lack of aftershocks.

4.4. Termination

The Kaikōura earthquake terminated near Cape Campbell, at the north-eastern tip of South Island. Surface ruptures were mapped on the Needles (offshore, but without rupture of the nearby/adjoining Boo Boo Fault (Kearse et al., 2018)), Marfells Beach, Cape Campbell Road and Lighthouse Faults (Litchfield et al., 2018). The rupture terminated despite the existence of multiple other pre-existing mapped faults in the region. The Cape Campbell region also hosted the 2013 Cook Strait earthquake sequence, including the M_W6.6 Cook Strait earthquake on July 21, 2013, and the subsequent M_W6.6 Lake Grassmere earthquake on August 16, 2013 (Hamling et al., 2014). This region is also close to the modeled southern rupture extend of the M8 1855 Wairarapa earthquake (Darby & Beanland, 1992; Rodgers & Little, 2006).

Dynamic rupture simulations have been able to simulate arrest on the Needles Fault (Ando & Kaneko, 2018; Ulrich et al., 2019), either by invoking a small (10° clockwise) rotation in the regional stress field (Ando & Kaneko, 2018), or by enforcing reduced pre-stress on the Needles Fault while rotating the stress field in the opposite direction (Ulrich et al., 2019). The two shallow (<25 km) S_{Hmax} estimations from Townend et al. (2012) in the region (their clusters 16 and 11) suggest a possible clockwise rotation as used by Ando and Kaneko (2018). The counter-clockwise rotated cluster in Cook Strait (cluster 18) has a centroid at 42 km depth and is likely related to stresses associated with subduction interface beneath. We therefore favor a clockwise rotation to an S_{Hmax} orientation of c. 110° which reduces the potential stress drop on the Needles Fault and leads to the spontaneous termination in the model of Ando and Kaneko (2018). This rotation is also consistent with the earlier work of Balfour et al. (2005).

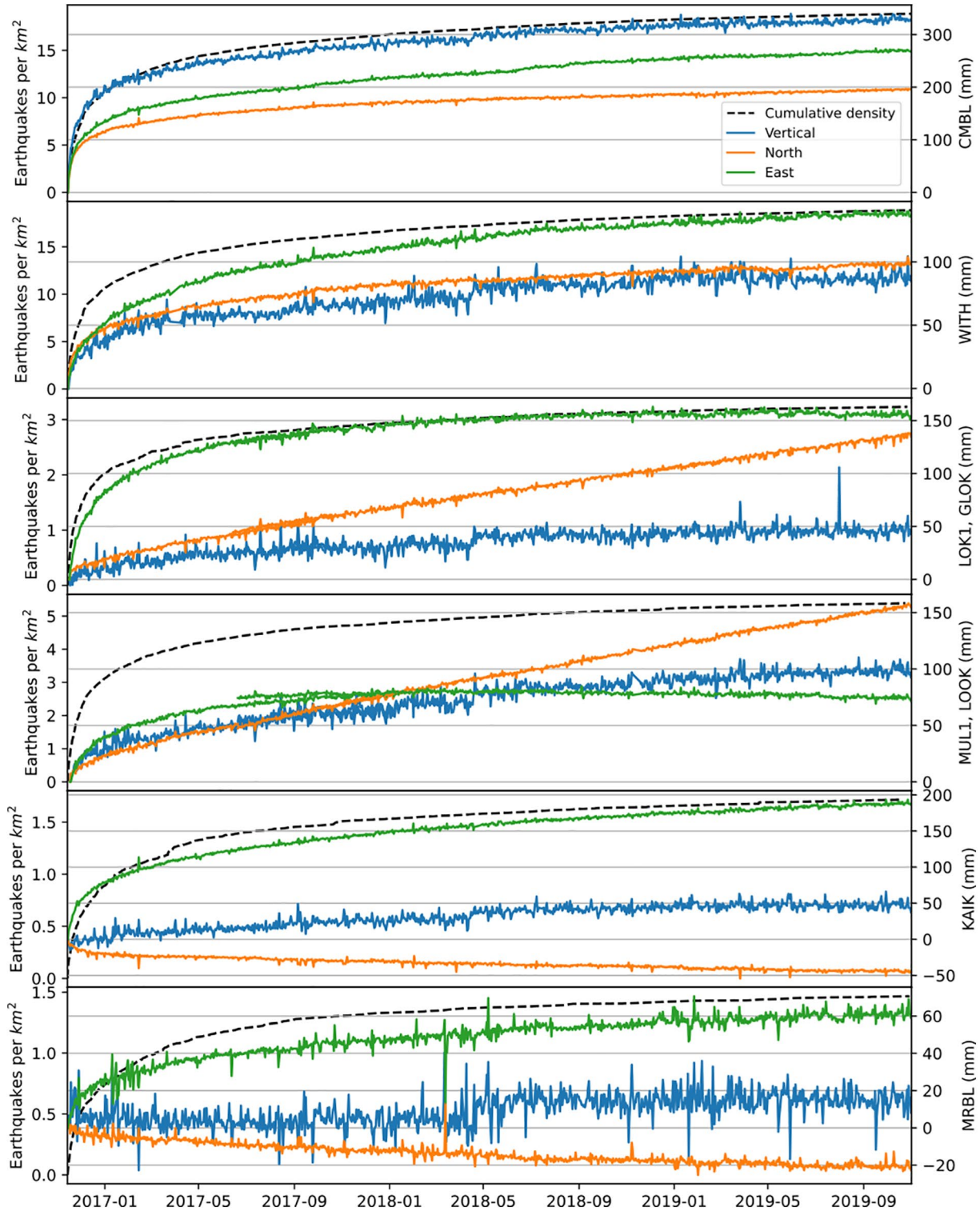

Figure 9. GPS time-series and cumulative aftershock density for regions around the Kaikōura afterslip region. Regions are ordered north (top) to south. GPS displacements for sites CMBL, WITH, KAIK and MRBL have a long-term gradient removed (calculated between 2015/01/01 to 2016/11/1). Sites LOK1, GLOK, MUL1 and LOOK have not had any gradient removed because they were not active prior to Kaikōura. Data from stations GLOK and LOOK have been shifted to have matching displacements at the end of the recording periods of LOK1 and MUL1 respectively. Note that the overlap is imperfect, but provides a representative view of displacement in the region. In general the evolution of the aftershock sequence matches the evolution of the displacement for these regions, however there are strong differences across the regions highlighting different amounts of afterslip.

Neither of the above-mentioned dynamic rupture models (Ando & Kaneko, 2018; Ulrich et al., 2019) includes slip on other faults around Cape Campbell, despite the mapped surface ruptures (Litchfield et al., 2018) and the diffuse aftershocks mapped here and by Lanza et al. (2019). Importantly, the inferred rupture plane of the Cook Strait earthquakes is rotated c. 9° clockwise of the average strike of the Needles Fault (Hamling et al., 2014), resulting in a more favorable orientation for slip on these faults in the regional stress-field. Interestingly we see a general paucity of earthquakes on the Needles Fault (Figure 8) compared to faults directly beneath Cape Campbell despite the co-seismic rupture of the Needles Fault. We suggest that this may be due to the unfavorable orientation of this fault. We also favor a more steeply dipping (near-vertical) Needles Fault, with much of the reverse component of deformation taken up by shallower dipping faults to the West.

Because the templates we use, despite having been constructed exclusively from aftershocks of the Kaikōura earthquake, detect aftershocks of the Cook Strait sequence (but not the mainshocks), the Kaikōura aftershock sequence must include re-rupture of favorably oriented faults that were active during the Cook Strait aftershock sequence. Focal mechanisms of aftershocks in this region include multiple dextral-reverse mechanisms striking c. 055°, similar to the Cook Strait mainshocks.

We consider two possibilities for the cause of the activation of the Cook Strait sequence fault(s) by the Kaikōura earthquake: (a) the Kaikōura earthquake co-seismically ruptured the more favorably oriented "Cook Strait Fault"; (b) seismicity on the "Cook Strait Fault" was triggered post-seismically. As computed by Ulrich et al. (2019), the maximum Coulomb failure stress (ΔCFS) reduction on the Needles Fault due to the Cook Strait sequence is small (c. 0.1 MPa), and is strongly heterogeneous. However, the stress drops on the "Cook Strait Fault" itself due to the Cook Strait and Lake Grassmere earthquakes are 1 and 3.5 MPa respectively. We hypothesize that this resulted in reduced pre-stress on the "Cook Strait Fault," ensuring that the Kaikōura earthquake could not generate significant rupture through this more favorably oriented fault, either co-seismically or post-seismically. Changes in frictional properties on the "Cook Strait Fault" may also act to inhibit rupture, but we have no direct observations of the frictional properties, nor how they vary in time for these faults.

Our aftershock locations do not show clear evidence for a structural boundary within Cook Strait as the control for rupture termination. Instead we observe a consistent migration of aftershocks away from the inferred rupture termination point into Cook Strait (see Section 4.5, Figures 7 and S9). Nevertheless, the aftershocks do concentrate within the region of low Q (high seismic attenuation), as demonstrated by Henrys et al. (2020). Henrys et al. (2020) suggested that the change in seismic properties in Cook Strait may be linked to changes in interface coupling, upper-plate deformation and strain-accumulation, which may play a role in rupture termination. In general the aftershocks are found to have occurred within regions of low Q, which may be indicative of regions of higher fracturing or damage, more capable of hosting seismicity (Henrys et al., 2020).

We suggest that a combination of an unfavorably oriented Needles Fault, reduced pre-stress due to prior rupture of other nearby faults, and the presence of diffuse faulting around Cape Campbell, served to terminate the rupture near Cape Campbell.

4.5. Post-Seismic

The catalog we present here is dominated by aftershocks providing important information on deformation processes following complex co-seismic slip. Spatially, several key features are apparent in the post-seismic period (Figure 7). First, the peak aftershock densities occur at the rupture termination point near Cape Campbell, and in the step-over region between the southern and northern rupture domains. Strong aftershock activity near rupture terminations where there are elevated stress concentrations is common (King et al., 1994), and we do see many aftershocks surrounding the Needles Fault (Figure 8): however, the majority of aftershocks around Cape Campbell occur in a distributed region between the Needles Fault and the location of the 2013 Cook Strait sequence. The patch of aftershocks around Cape Campbell expands in time, following a roughly log-time expansion, and seems to expand bilaterally (Figures 7 and S9).

As previously reported, there are very few aftershocks associated with the Papatea Fault and the highest-slip patch of the Kekerengu Fault, which we interpret to be segments that experienced near-total stress-drop.

The high-slip patch of the Kekerengu Fault separates the two regions of high aftershock density and may provide a limiting control to the aftershock sequence.

In the south, we see a continuation of aftershocks beyond the southern rupture termination point, and clustered triggered off-fault seismicity. We also note that, although there are aftershocks on the Leader and surrounding faults, we also see a continuous trend of aftershocks joining the Humps and Hundalee Faults, effectively cutting off this block, and potentially accommodating block rotation as proposed by T. Wang et al. (2020).

Comparison of GNSS displacements with earthquake rates in regions surrounding the GNSS site shows that aftershock rates are generally proportional to displacement rates (Figure 9). The catalog presented here is sufficiently detailed to map earthquakes to individual faults, but the published post-seismic slip models do not have sufficiently detailed crustal fault resolution to directly compare aftershocks with afterslip. Because of the complexity of the earthquake, GNSS displacement measured at a single site is likely to correspond to slip on multiple fault sources, rendering direct comparison of geodetic data with seismicity non-unique. Nevertheless, despite the range of faulting and co-seismic slip, it appears that aftershock distributions correlate well with geodetically determined displacements, suggesting that aftershocks are driven by local afterslip (Frank et al., 2017; Perfettini et al., 2018).

5. Conclusions

The 2016 M 7.8 Kaikōura earthquake is widely regarded as one of the most complex earthquakes in recorded history (Hamling, 2020). Detailed mapping of seismicity around the faults that ruptured in the Kaikōura earthquake further emphasizes this complexity: at-least in the post-seismic period, multiple faults that did not have surface rupture are activated including two of the high slip-rate and high hazard Marlborough Faults (the Clarence and the Hope Faults). However, the additional faults observable through this mapping may also simplify some of the kinematics of the rupture by providing additional structures to host variations in slip between nearby fault segments.

To address the original outstanding questions outlined in Section 1.3, and as discussed in Sections 4.1–4.5, our conclusions are as follows:

1. The mainshock unequivocally nucleated on the Humps Fault. Previous scatter in published locations can be attributed to inappropriate location methods or data quality issues which we have thoroughly addressed in this study.
2. We do not observe any precursory activity in our catalog, but this is likely in-part a limitation of using the aftershock-derived template set. We do observe one foreshock 7 s prior to the mainshock, however the sparsity of seismic stations limits our ability to investigate further.
3. Offshore thrust faulting illuminated by aftershocks suggests a physical connection between the Hundalee and Papatea Faults, which may explain anomalously high slip on the Papatea Fault and provides a likely southern/offshore rupture route.
4. The Snowgrass Creek-Papatea-Jordan Thurst-Kekerengu system acts as a quadruple junction providing a means of distributing the drop in slip between the Kekerengu and Jordan Thrust Faults.
5. Both the Hope and Clarence Faults were active post-seismically and produced aftershocks, though these were not laterally extensive, and occur near fault junctions or transitional zones.
6. We observe very few aftershocks on the subduction interface. A proportion of the afterslip previously mapped onto the subduction interface may instead be accommodated by unmodelled upper crustal faults, such as the previously unidentified Snowgrass Creek Fault, the Clarence Fault and diffuse faulting characterized by abundant aftershocks near Cape Campbell. However crustal faults are unlikely to remove the need for deep deformation to explain the long-wavelength signature in the geodetic data, but this deformation likely occurs aseismically.
7. The rupture terminated near the epicenters of the Lake Grassmere and Cook Strait 2013 earthquakes, and likely re-ruptured these faults. The Cook Strait and Lake Grassmere faults are more favorably oriented for slip than the co-seismically ruptured Needles Fault, and we propose that the combination of unfavorable orientation of the Needles together with reduced pre-stress on the Lake Grassmere and Cook Strait faults was sufficient to cause the rupture to terminate here.

8. Aftershocks concentrate at step-overs in faulting, and at the rupture termination near Cape Campbell. The patch of high co-seismic slip on the Kekerengu Fault has few aftershocks and potentially experienced near total stress drop, and may separate patches of afterslip reducing aftershock productivity.

Considering all of the above, we infer that the Kaikōura earthquake nucleated without significant detectable precursory seismicity on the Humps Fault before transitioning through the Leader/Stone Jug system and onto the Hundalee Fault. The rupture then continued directly onto the offshore fault system characterized by reverse slip, elsewhere called the Point Keen Fault. Slip then transitioned onto the Papatea Fault, likely by directly linked faults at depth in a thrust block bounded by sinistral faulting on the Papatea and Snowgrass Creek Faults (Figure 6). Within this block, the Jordan Thrust Fault was reactivated in an extensional stress regime giving rise to normal motion (in contrast to the long-term motion on this fault), and the difference in slip between the Jordan Thrust and Kekerengu Faults is accommodated by buried slip on the previously unknown Snowgrass Creek Fault.

Slip then transitioned onto the Kekerengu Fault, which experienced near-total stress-drop in the high slip patch identified by other authors (e.g., Kearse et al., 2018), and characterized here by a lack of aftershocks. The rupture then propagated onto the Needles Fault and other faults around Cape Campbell that were previously ruptured in the 2013 Cook Strait earthquakes. A combination of an unfavorable stress orientation on the Needles Fault and reduced pre-stress due to recent slip on the Cook Strait and Lake Grassmere faults resulted in the termination of the Kaikōura earthquake at Cape Campbell. We see no evidence for seismic slip on an underlying subduction interface, apart from a small cluster of interface related seismicity near Cape Campbell. We therefore suggest that the boundary between the overriding Australian plate and subduction Pacific plate may be ductile beneath much of the Kaikōura earthquake fault system as suggested by Eberhart-Phillips et al. (2021).

Acknowledgments
Chamberlain and Townend are grateful to New Zealand's Earthquake Commission (EQC) for funding through the EQC Programme in Seismology and Tectonic Geodesy at Victoria University of Wellington, and an EQC Biennial Grant (18/753), and to the Royal Society of New Zealand for funding through the Marsden Fast-Start project 17-VUW-121. Frank, Townend and Chamberlain also received funding for this collaboration through the New Zealand Royal Societies Catalyst Grant scheme. Chamberlain and Warren-Smith are grateful to the New Zealand Ministry of Business, Innovation and Employment for funding through the Endeavour programme: 'Rapid Characterisation of Earthquakes and Tsunamis (RCET)'. Warren-Smith was funded through GNS Science Ministy of Business Innovation and Employment strategic science investment funding (GNS-SSIF). Initial compute time was provided by the New Zealand eScience Infrastructure (NeSI) for which we are grateful. Later computations were run on Amazon Web Services, with data handling assistance from GeoNet. We acknowledge the New Zealand GeoNet project and its sponsors EQC, GNS Science, LINZ, NEMA and MBIE for providing data used in this study. ObsPy (Krischer et al., 2015) was used extensively throughout this work, figures were made using matplotlib (Hunter, 2007) and cartopy (Met Office, 2010–2015), and we are very grateful to the developers and maintainers of these open-source projects who enable complex science. We are grateful to the Editor, Rachel Abercrombie, Daniel Trugman and Thorne Lay for their helpful reviews. Finally we are grateful to Tim Little, Andy Howell, Carolyn Boulton, James Crampton, Rob Langridge, Laura Wallace, Ian Hamling and others in the New Zealand geoscience community for informative discussions during the preparation of this work.

Data Availability Statement

All waveform data for GeoNet stations were downloaded from GeoNet via their FDSN client (last accessed April 20, 2021). All data from the STREWN network (code Z1) were downloaded from the IRIS FDSN Client (last accessed 6 June 2021). The catalog generated here is available at https://doi.org/10.5281/zenodo.4717333 (last accessed April 24, 2021) in QUAKEML and CSV format. All code used to generate this catalog is open-source, and the scripts to complete the workflow are available on at https://zenodo.org/record/5047794#.YNzESzp5bLo (last accessed July 1, 2021).

References

Ando, R., & Kaneko, Y. (2018). Dynamic rupture simulation reproduces spontaneous multifault rupture and arrest during the 2016 Mw 7.9 Kaikōura earthquake. *Geophysical Research Letters*, *45*(23), 875–12. https://doi.org/10.1029/2018GL080550

Bai, Y., Lay, T., Cheung, K. F., & Ye, L. (2017). Two regions of seafloor deformation generated the tsunami for the 13 November 2016, Kaikōura, New Zealand earthquake. *Geophysical Research Letters*, *44*(13), 6597–6606. https://doi.org/10.1002/2017GL073717

Balfour, N., Savage, M., & Townend, J. (2005). Stress and crustal anisotropy in Marlborough, New Zealand: Evidence for low fault strength and structure-controlled anisotropy. *Geophysical Journal International*, *163*(3), 1073–1086. https://doi.org/10.1111/j.1365-246x.2005.02783.x

Beaucé, E., Frank, W. B., & Romanenko, A. (2018). Fast matched filter (FMF): An efficient seismic matched-filter search for both CPU and GPU architectures. *Seismological Research Letters*, *89*(1), 165–172. https://doi.org/10.1785/0220170181

Bradley, B. A., Razafindrakoto, H. N., & Polak, V. (2017). Ground-motion observations from the 14 November 2016 M w 7.8 Kaikōura, New Zealand, earthquake and insights from broadband simulations. *Seismological Research Letters*, *88*(3), 740–756. https://doi.org/10.1785/0220160225

Bratt, S., & Nagy, W. (1991). *The LocSAT program*. Science Applications International Corporation.

Cesca, S., Zhang, Y., Mouslopoulou, V., Wang, R., Saul, J., Savage, M., et al. (2017). Complex rupture process of the Mw 7.8, 2016, Kaikōura earthquake, New Zealand, and its aftershock sequence. *Earth and Planetary Science Letters*, *478*, 110–120. https://doi.org/10.1016/j.epsl.2017.08.024

Chamberlain, C. J., Hopp, C. J., Boese, C. M., Warren-Smith, E., Chambers, D., Chu, S. X., et al. (2018). EQcorrscan: Repeating and near-repeating earthquake detection and analysis in python. *Seismological Research Letters*, *89*(1), 173–181. https://doi.org/10.1785/0220170151

Chamberlain, C. J., Townend, J., & Gerstenberger, M. C. (2020). RT-EQcorrscan: Near-real-time matched-filtering for rapid development of dense earthquake catalogs. *Seismological Society of America*, *91*(6), 3574–3584. https://doi.org/10.1785/0220200171

Christophersen, A., Rhoades, D., Gerstenberger, M., Bannister, S., Becker, J., Potter, S., & McBride, S. (2017). Progress and challenges in operational earthquake forecasting in New Zealand. In *New Zealand society for earthquake engineering annual technical conference*.

Clark, K., Nissen, E., Howarth, J., Hamling, I., Mountjoy, J., Ries, W., et al. (2017). Highly variable coastal deformation in the 2016 MW7.8 Kaikura earthquake reflects rupture complexity along a transpressional plate boundary. *Earth and Planetary Science Letters*, *474*, 334–344. https://doi.org/10.1016/j.epsl.2017.06.048

Darby, D. J., & Beanland, S. (1992). Possible source models for the 1855 Wairarapa earthquake, New Zealand. *Journal of Geophysical Research: Solid Earth*, *97*(B9), 12375–12389. https://doi.org/10.1029/92jb00567

Diederichs, A., Nissen, E., Lajoie, L., Langridge, R., Malireddi, S., Clark, K., et al. (2019). Unusual kinematics of the Papatea fault (2016 Kaikōura earthquake) suggest anelastic rupture. *Science advances*, *5*(10), eaax5703. https://doi.org/10.1126/sciadv.aax5703

Eberhart-Phillips, D., & Bannister, S. (2015). 3-D imaging of the northern Hikurangi subduction zone, New Zealand: Variations in subducted sediment, slab fluids and slow slip. *Geophysical Journal International*, *201*(2), 838–855. https://doi.org/10.1093/gji/ggv057

Eberhart-Phillips, D., Bannister, S., & Reyners, M. (2017). *New Zealand wide model 2.1 seismic velocity model for New Zealand*. Zenodo. https://doi.org/10.5281/zenodo.1043558

Eberhart-Phillips, D., Ellis, S., Lanza, F., & Bannister, S. (2021). Heterogeneous material properties–As inferred from seismic attenuation - Influenced multiple fault rupture and ductile creep of the Kaikōura Mw 7.8 earthquake, New Zealand. *Geophysical Journal International*. https://doi.org/10.1093/gji/ggab272

Frank, W. B., Poli, P., & Perfettini, H. (2017). Mapping the rheology of the Central Chile subduction zone with aftershocks. *Geophysical Research Letters*, *44*(11), 5374–5382. https://doi.org/10.1002/2016gl072288

Frigo, M., & Johnson, S. G. (1998). FFTW: An adaptive software architecture for the FFT. In *Proceedings of the 1998 Ieee International Conference on Acoustics, Speech and Signal Processing, Icassp'98 (cat. no. 98ch36181)* (Vol. *3*, pp. 1381–1384).

Gusman, A. R., Satake, K., Gunawan, E., Hamling, I., & Power, W. (2018). Contribution from multiple fault ruptures to tsunami generation during the 2016 Kaikōura earthquake. *Pure and Applied Geophysics*, *175*(8), 2557–2574. https://doi.org/10.1007/s00024-018-1949-z

Hainzl, S. (2016). Rate-dependent incompleteness of earthquake catalogs. *Seismological Research Letters*, *87*(2A), 337–344. https://doi.org/10.1785/0220150211

Hamling, I. J. (2020). A review of the 2016 Kaikura earthquake: Insights from the first 3 years. *Journal of the Royal Society of New Zealand*, *50*(2), 226–244. https://doi.org/10.1080/03036758.2019.1701048

Hamling, I. J., D'Anastasio, E., Wallace, L. M., Ellis, S., Motagh, M., Samsonov, S., et al. (2014). Crustal deformation and stress transfer during a propagating earthquake sequence: The 2013 Cook Strait sequence, central New Zealand. *Journal of Geophysical Research: Solid Earth*, *119*(7), 6080–6092. https://doi.org/10.1002/2014JB011084

Hamling, I. J., Hreinsdóttir, S., Clark, K., Elliott, J., Liang, C., Fielding, E., et al. (2017). Complex multifault rupture during the 2016 Mw 7.8 Kaikōura earthquake, New Zealand. *Science*, *356*(6334), eaam7194. https://doi.org/10.1126/science.aam7194

Harris, R. A., Archuleta, R. J., & Day, S. M. (1991). Fault steps and the dynamic rupture process: 2-D numerical simulations of a spontaneously propagating shear fracture. *Geophysical Research Letters*, *18*(5), 893–896. https://doi.org/10.1029/91gl01061

Henrys, S., Eberhart-Phillips, D., Bassett, D., Sutherland, R., Okaya, D., Savage, M., & others. (2020). Upper plate heterogeneity along the Southern Hikurangi Margin, New Zealand. *Geophysical Research Letters*, *47*(4), e2019GL085511. https://doi.org/10.1029/2019gl085511

Holden, C., Kaneko, Y., D'Anastasio, E., Benites, R., Fry, B., & Hamling, I. J. (2017). The 2016 Kaikura earthquake revealed by kinematic source inversion and seismic wavefield simulations: Slow rupture propagation on a geometrically complex crustal fault network. *Geophysical Research Letters*, *44*(22), 11320–11328. https://doi.org/10.1002/2017GL075301

Howell, A., Nissen, E., Stahl, T., Clark, K., Kearse, J., Van Dissen, R., et al. (2020). Three-dimensional surface displacements during the 2016 MW 7.8 Kaikura earthquake (New Zealand) from photogrammetry-derived point clouds. *Journal of Geophysical Research: Solid Earth*, *125*(1), e2019JB018739. https://doi.org/10.1029/2019JB018739

Hunter, J. D. (2007). Matplotlib: A 2D graphics environment. *Computing in Science & Engineering*, *9*(3), 90–95. https://doi.org/10.1109/MCSE.2007.55

Illsley-Kemp, F., Barker, S. J., Wilson, C. J., Chamberlain, C. J., Hreinsdóttir, S., Ellis, S., et al. (2021). Volcanic unrest at Taupō volcano in 2019: Causes, mechanisms and implications. *Geochemistry, Geophysics, Geosystems*, *22*, e2021GC009803. https://doi.org/10.1029/2021GC009803

Kaiser, A., Balfour, N., Fry, B., Holden, C., Litchfield, N., Gerstenberger, M., et al. (2017). The 2016 Kaikura, New Zealand, earthquake: Preliminary seismological report. *Seismological Research Letters*, *88*(3), 727–739. https://doi.org/10.1785/0220170018

Kearse, J., Little, T. A., Van Dissen, R. J., Barnes, P. M., Langridge, R., Mountjoy, J., et al. (2018). Onshore to offshore ground-surface and seabed rupture of the Jordan–Kekerengu–Needles fault network during the 2016 Mw 7.8 Kaikura earthquake, New Zealand. *Bulletin of the Seismological Society of America*, *108*(3B), 1573–1595. https://doi.org/10.1785/0120170304

Kennett, B., & Engdahl, E. (1991). Traveltimes for global earthquake location and phase identification. *Geophysical Journal International*, *105*(2), 429–465. https://doi.org/10.1111/j.1365-246x.1991.tb06724.x

King, G. C., Stein, R. S., & Lin, J. (1994). Static stress changes and the triggering of earthquakes. *Bulletin of the Seismological Society of America*, *84*(3), 935–953.

Klinger, Y., Okubo, K., Vallage, A., Champenois, J., Delorme, A., Rougier, E., et al. (2018). Earthquake damage patterns resolve complex rupture processes. *Geophysical Research Letters*, *45*(19), 10–279. https://doi.org/10.1029/2018gl078842

Krischer, L., Megies, T., Barsch, R., Beyreuther, M., Lecocq, T., Caudron, C., & Wassermann, J. (2015). ObsPy: A bridge for seismology into the scientific Python ecosystem. *Computational Science & Discovery*, *8*(1), 014003. https://doi.org/10.1088/1749-4699/8/1/014003

Lamb, S., Arnold, R., & Moore, J. D. (2018). Locking on a megathrust as a cause of distributed faulting and fault-jumping earthquakes. *Nature Geoscience*, *11*(11), 871–875. https://doi.org/10.1038/s41561-018-0230-5

Langridge, R., Ries, W., Litchfield, N., Villamor, P., Van Dissen, R., Barrell, D., et al. (2016). The New Zealand active faults database. *New Zealand Journal of Geology and Geophysics*, *59*(1), 86–96. https://doi.org/10.1080/00288306.2015.1112818

Langridge, R. M., Rowland, J., Villamor, P., Mountjoy, J., Townsend, D. B., Nissen, E., et al. (2018). Coseismic rupture and preliminary slip estimates for the Papatea fault and its role in the 2016 Mw7.8 Kaikura, New Zealand, earthquake. *Bulletin of the Seismological Society of America*, *108*(3B), 1596–1622. https://doi.org/10.1785/0120170336

Lanza, F., Chamberlain, C. J., Jacobs, K., Warren-Smith, E., Godfrey, H. J., Kortink, M., et al. (2019). Crustal fault connectivity of the Mw 7.8 2016 Kaikura Earthquake constrained by aftershock relocations. *Geophysical Research Letters*, *46*(12), 6487–6496. https://doi.org/10.1029/2019GL082780

Lienert, B. R., & Havskov, J. (1995). A computer program for locating earthquakes both locally and globally. *Seismological Research Letters*, *66*(5), 26–36. https://doi.org/10.1785/gssrl.66.5.26

Litchfield, N. J., Villamor, P., Dissen, R. J. V., Nicol, A., Barnes, P. M., Barrell, A., et al. (2018). Surface rupture of multiple crustal faults in the 2016 M w 7.8 Kaikōura, New Zealand, Earthquake. *Bulletin of the Seismological Society of America*, *108*(3B), 1496–1520. https://doi.org/10.1785/0120170300

Liu, C., Lay, T., Brodsky, E. E., Dascher-Cousineau, K., & Xiong, X. (2019). Coseismic rupture process of the large 2019 ridgecrest earthquakes from joint inversion of geodetic and seismological observations. *Geophysical Research Letters*, *46*(21), 11820–11829. https://doi.org/10.1029/2019GL084949

Lomax, A., Virieux, J., Volant, P., & Berge-Thierry, C. (2000). Probabilistic earthquake location in 3D and layered models. In *Advances in seismic event location* (pp. 101–134). Springer. https://doi.org/10.1007/978-94-015-9536-0_5

Met Office. (2010–2015). *Cartopy: A cartographic python library with a Matplotlib interface [computer software manual]. Exeter, Devon*. Retrieved from https://scitools.org.uk/cartopy

Michailos, K., Smith, E. G., Chamberlain, C. J., Savage, M. K., & Townend, J. (2019). Variations in seismogenic thickness along the Central Alpine Fault, New Zealand, revealed by a decade's relocated microseismicity. *Geochemistry, Geophysics, Geosystems*, *20*(1), 470–486. https://doi.org/10.1029/2018gc007743

Mouslopoulou, V., Saltogianni, V., Nicol, A., Oncken, O., Begg, J., Babeyko, A., et al. (2019). Breaking a subduction-termination from top to bottom: The large 2016 Kaikura Earthquake, New Zealand. *Earth and Planetary Science Letters*, *506*, 221–230. https://doi.org/10.1016/j.epsl.2018.10.020

Nicol, A., Khajavi, N., Pettinga, J. R., Fenton, C., Stahl, T., Bannister, S., et al. (2018). Preliminary geometry, displacement, and kinematics of fault ruptures in the epicentral region of the 2016 Mw 7.8 Kaikura, New Zealand, Earthquake. *Bulletin of the Seismological Society of America*, *108*(3B), 1521–1539. https://doi.org/10.1785/0120170329

Okada, T., Iio, Y., Matsumoto, S., Bannister, S., Ohmi, S., Horiuchi, S., et al. (2019). Comparative tomography of reverse-slip and strike-slip seismotectonic provinces in the northern South Island, New Zealand. *Tectonophysics*, *765*, 172–186. https://doi.org/10.1016/j.tecto.2019.03.016

Peng, Z., Fry, B., Chao, K., Yao, D., Meng, X., & Jolly, A. (2018). Remote triggering of microearthquakes and tremor in New Zealand following the 2016 Mw 7.8 Kaikura Earthquake. *Bulletin of the Seismological Society of America*, *108*(3B), 1784–1793. https://doi.org/10.1785/0120170327

Perfettini, H., Frank, W., Marsan, D., & Bouchon, M. (2018). A model of aftershock migration driven by afterslip. *Geophysical Research Letters*, *45*(5), 2283–2293. https://doi.org/10.1002/2017gl076287

Plesch, A., Shaw, J. H., Ross, Z. E., & Hauksson, E. (2020). Detailed 3D fault representations for the 2019 Ridgecrest, California, earthquake sequence. *Bulletin of the Seismological Society of America*, *110*(4), 1818–1831. https://doi.org/10.1785/0120200053

Rattenbury, M., & Isaac, M. (2012). The QMAP 1: 250 000 geological map of New Zealand project. *New Zealand Journal of Geology and Geophysics*, *55*(4), 393–405. https://doi.org/10.1080/00288306.2012.725417

Ristau, J. (2013). Update of regional moment tensor analysis for earthquakes in New Zealand and adjacent offshore regions. *Bulletin of the Seismological Society of America*, *103*(4), 2520–2533. https://doi.org/10.1785/0120120339

Rodgers, D., & Little, T. (2006). World's largest coseismic strike-slip offset: The 1855 rupture of the Wairarapa Fault, New Zealand, and implications for displacement/length scaling of continental earthquakes. *Journal of Geophysical Research: Solid Earth*, *111*(B12), B12408. https://doi.org/10.1029/2005jb004065

Romanet, P., & Ide, S. (2019). Ambient tectonic tremors in Manawatu, Cape Turnagain, Marlborough, and Puysegur, New Zealand. *Earth, Planets and Space*, *71*(1), 1–9. https://doi.org/10.1186/s40623-019-1039-1

Senobari, N. S., Funning, G. J., Keogh, E., Zhu, Y., Yeh, C.-C. M., Zimmerman, Z., & Mueen, A. (2019). Super-efficient cross-correlation (SEC-C): A fast matched filtering code suitable for desktop computers. *Seismological Research Letters*, *90*(1), 322–334. https://doi.org/10.1785/0220180122

Stirling, M., McVerry, G., Gerstenberger, M., Litchfield, N., Van Dissen, R., Berryman, K., et al. (2012). National seismic hazard model for New Zealand: 2010 update. *Bulletin of the Seismological Society of America*, *102*(4), 1514–1542. https://doi.org/10.1785/0120110170

Tan, F., Ge, Z., Kao, H., & Nissen, E. (2019). Validation of the 3-D phase-weighted relative back projection technique and its application to the 2016 M w 7.8 Kaikōura Earthquake. *Geophysical Journal International*, *217*(1), 375–388. https://doi.org/10.1093/gji/ggz032

Townend, J., Sherburn, S., Arnold, R., Boese, C., & Woods, L. (2012). Three-dimensional variations in present-day tectonic stress along the Australia–Pacific plate boundary in New Zealand. *Earth and Planetary Science Letters*, *353*, 47–59. https://doi.org/10.1016/j.epsl.2012.08.003

Trugman, D. T., & Shearer, P. M. (2017). GrowClust: A hierarchical clustering algorithm for relative earthquake relocation, with application to the Spanish Springs and Sheldon, Nevada, earthquake sequences. *Seismological Research Letters*, *88*(2A), 379–391. https://doi.org/10.1785/0220160188

Ulrich, T., Gabriel, A.-A., Ampuero, J.-P., & Xu, W. (2019). Dynamic viability of the 2016 Mw 7.8 Kaikōura earthquake cascade on weak crustal faults. *Nature Communications*, *10*(1), 375–388. https://doi.org/10.1038/s41467-019-09125

Van Dissen, R., & Nicol, A. (2009). Mid-late Holocene paleoseismicity of the eastern Clarence Fault, Marlborough, New Zealand. *New Zealand Journal of Geology and Geophysics*, *52*(3), 1213. https://doi.org/10.1080/00288300909509886

Van Dissen, R., & Yeats, R. S. (1991). Hope fault, Jordan thrust, and uplift of the seaward Kaikōura Range, New Zealand. *Geology*, *19*(4), 393–396. https://doi.org/10.1130/0091-7613(1991)019<0393:hfjtau>2.3.co;2

Waldhauser, F., & Ellsworth, W. L. (2000). A double-difference earthquake location algorithm: Method and application to the northern Hayward fault, California. *Bulletin of the Seismological Society of America*, *90*(6), 1353–1368. https://doi.org/10.1785/0120000006

Wallace, L. M., Hreinsdóttir, S., Ellis, S., Hamling, I., D'Anastasio, E., & Denys, P. (2018). Triggered slow slip and afterslip on the southern hikurangi subduction zone following the Kaikura Earthquake. *Geophysical Research Letters*, *45*(10), 4710–4718. https://doi.org/10.1002/2018GL077385

Wallace, L. M., Kaneko, Y., Hreinsdóttir, S., Hamling, I., Peng, Z., Bartlow, N., et al. (2017). Large-scale dynamic triggering of shallow slow slip enhanced by overlying sedimentary wedge. *Nature Geoscience*, *10*, 765–770. https://doi.org/10.1038/NGEO3021

Walsh, D., Arnold, R., & Townend, J. (2009). A Bayesian approach to determining and parametrizing earthquake focal mechanisms. *Geophysical Journal International*, *176*(1), 235–255. https://doi.org/10.1111/j.1365-246x.2008.03979.x

Wang, D., Chen, Y., Wang, Q., & Mori, J. (2018). Complex rupture of the 13 November 2016 Mw 7.8 Kaikōura, New Zealand earthquake: Comparison of high-frequency and low-frequency observations. *Tectonophysics*, *733*, 100–107. https://doi.org/10.1016/j.tecto.2018.02.004

Wang, T., Jiao, L., Tapponnier, P., Shi, X., & Wei, S. (2020). Space imaging geodesy reveals near circular, coseismic block rotation during the 2016 Mw 7.8 Kaikōura earthquake, New Zealand. *Geophysical Research Letters*, *47*(22), e2020GL090206. https://doi.org/10.1029/2020gl090206

Wang, T., Wei, S., Shi, X., Qiu, Q., Li, L., Peng, D., et al. (2018). The 2016 Kaikōura earthquake: Simultaneous rupture of the subduction interface and overlying faults. *Earth and Planetary Science Letters*, *482*, 44–51. https://doi.org/10.1016/j.epsl.2017.10.056

Warren-Smith, E., Chamberlain, C. J., Lamb, S., & Townend, J. (2017). High-precision analysis of an aftershock sequence using matched-filter detection: The 4 May 2015 ML 6 Wanaka earthquake, Southern Alps, New Zealand. *Seismological Research Letters*, *88*(4), 1065–1077.

Wesnousky, S. G. (2006). Predicting the endpoints of earthquake ruptures. *Nature*, *444*(7117), 358–360. https://doi.org/10.1038/nature05275

Wiemer, S., & Wyss, M. (2000). Minimum magnitude of completeness in earthquake catalogs: Examples from Alaska, the western United States, and Japan. *Bulletin of the Seismological Society of America*, *90*(4), 859–869. https://doi.org/10.1785/0119990114

Williams, C. A., Eberhart-Phillips, D., Bannister, S., Barker, D. H. N., Henrys, S., Reyners, M., & Sutherland, R. (2013). Revised interface geometry for the Hikurangi subduction zone, New Zealand. *Seismological Research Letters*, *84*(6), 1066–1073. https://doi.org/10.1785/0220130035

Williams, J. N., Barrell, D. J. A., Stirling, M. W., Sauer, K. M., Duke, G. C., & Hao, K. X. (2018). Surface rupture of the Hundalee Fault during the 2016 Mw 7.8 Kaikura earthquake. *Bulletin of the Seismological Society of America*, *06*(3B), 1540–1555. https://doi.org/10.1785/0120170291

Xu, W., Feng, G., Meng, L., Zhang, A., Ampuero, J. P., Bürgmann, R., & Fang, L. (2018). Transpressional rupture cascade of the 2016 Mw 7.8 Kaikōura earthquake, New Zealand. *Journal of Geophysical Research: Solid Earth*, *123*(3), 2396–2409. https://doi.org/10.1002/2017JB015168

Yao, D., Peng, Z., Kaneko, Y., Fry, B., & Meng, X. (2021). Dynamic triggering of earthquakes in the North Island of New Zealand following the 2016 Mw 7.8 Kaikōura earthquake. *Earth and Planetary Science Letters*, *557*, 116723. https://doi.org/10.1016/j.epsl.2020.116723

Yu, C., Li, Z., & Penna, N. T. (2020). Triggered afterslip on the southern Hikurangi subduction interface following the 2016 Kaikōura earthquake from InSAR time series with atmospheric corrections. *Remote Sensing of Environment*, *251*, 112097. https://doi.org/10.1016/j.rse.2020.112097

Zinke, R., Hollingsworth, J., Dolan, J. F., & Van Dissen, R. (2019). Three-dimensional surface deformation in the 2016 MW 7.8 Kaikōura, New Zealand, earthquake from optical image correlation: Implications for strain localization and long-term evolution of the Pacific-Australian plate boundary. *Geochemistry, Geophysics, Geosystems*, *20*(3), 1609–1628. https://doi.org/10.1029/2018gc007951